

RESEARCH ARTICLE

10.1029/2018JF004778

Key Points:

- We simulate a large historical landslide-dam outburst flood using 2-D shallow water equations over 400 km through rugged Himalayan topography
- GeoClaw simulations are consistent with field and remote observations of high-water marks, deposits, landslides, and reported peak discharge
- Results improve hazard prediction and understanding of bedrock incision, sediment transport, and deposition during outburst floods

Supporting Information:

- Supporting Information S1
- Supporting Information S2
- Supporting Information S3
- Movie S1
- Movie S2
- Movie S3
- Movie S4
- Movie S5
- Movie S6
- Movie S7
- Movie S8
- Data Set S1
- Data Set S2

Correspondence to:

M. D. Turzewski and K. W. Huntington,
zewski@uw.edu;
kate1@uw.edu

Citation:

Turzewski, M. D., Huntington, K. W., & LeVeque, R. J. (2019). The geomorphic impact of outburst floods: Integrating observations and numerical simulations of the 2000 Yigong flood, eastern Himalaya. *Journal of Geophysical Research: Earth Surface*, *124*, 1056–1079. <https://doi.org/10.1029/2018JF004778>

Received 31 MAY 2018

Accepted 26 MAR 2019

Accepted article online 1 APR 2019

Published online 1 MAY 2019

©2019. American Geophysical Union.
All Rights Reserved.

The Geomorphic Impact of Outburst Floods: Integrating Observations and Numerical Simulations of the 2000 Yigong Flood, Eastern Himalaya

Michael D. Turzewski¹ , Katharine W. Huntington¹ , and Randall J. LeVeque² 

¹Department of Earth and Space Sciences, University of Washington, Seattle, WA, USA, ²Department of Applied Mathematics, University of Washington, Seattle, WA, USA

Abstract Outburst floods in mountainous landscapes traverse complex topography and interact with the channel and valley walls, producing intense flow hydraulics that drive geomorphic change and impact people and infrastructure. Evidence of modern and ancient outburst floods is scattered around the eastern Himalaya, but hydraulics related to these geomorphic features are uncharacterized, limiting our understanding of the role of large floods in long-term evolution of the region. Here we combine remote and field observations of the 2000 Yigong River landslide-dam outburst flood with 2-D numerical flood simulations using the software GeoClaw. Modeling results agree with field evidence to the extent that we judge the simulated hydraulics to be relevant to flood hazard and geomorphic investigations. Results show that the hydraulics of outburst floods through rugged topography differ from those expected for nonflood flows, in magnitude and in the spatial patterns of flow speed, direction, and shear stress. The flood produced sustained high bed shear stresses capable of plucking meter-scale blocks immediately downstream of breach, in the steep Tsangpo Gorge, and in isolated locations associated with valley constrictions. Simulated shear stresses suggest that outburst floods deposited numerous kilometer-scale boulder bars observed along the flood pathway, armoring the bed, increasing channel roughness, and inhibiting incision in locations that would not be predicted for nonflood flows. Our findings highlight the potential for different magnitude flows to promote not only different amounts, but also different patterns of bedrock erosion, with implications for the role of prehistoric megafloods in the topographic evolution of the eastern Himalaya.

1. Introduction

High-magnitude ($>10^5$ m³/s) lake outburst floods can dramatically alter landscapes and greatly impact human lives and infrastructure. Yet links between spatial patterns of flood hydraulics and geomorphic observations are lacking for some of the largest, most devastating historical outburst floods (e.g., Hewitt, 1968; O'Connor et al., 2013), and for many of the largest ancient outburst megafloods ($>10^6$ m³/s) that have occurred on Earth (e.g., Baker, 1973; Baynes et al., 2015; Bretz, 1923; Carling, 1996a, 1996b; Lamb, Dietrich, Aciego, et al., 2008; Malde, 1968; Montgomery et al., 2004; O'Connor, 1993) and on Mars (Baker, 2001; Baker & Milton, 1974; Chapman et al., 2003; Goudge & Fassett, 2018). Opportunities are rare to study outburst floods and their geomorphic consequences (Cook et al., 2018; Lamb & Fongstad, 2010). As a result, questions remain regarding the net impact of outburst floods on landscapes, particularly in mountainous settings where the interaction of flood hydraulics with valley topography is complex.

In the eastern Himalaya, abundant evidence for valley blockage by glacial and landslide dams (Chen et al., 2008; Guangxiang & Xitao, 2007; Guangxiang & Qingli, 2012; Huang et al., 2014; Hu et al., 2018; Korup & Montgomery, 2008; Korup et al., 2010; Zhu & Li, 2000)—some with downstream evidence of flooding—suggests that catastrophic outburst floods may have been common throughout the Quaternary. Such evidence has led workers to propose a variety of models for the role of outburst floods in deposition and channel incision, particularly in the steep and rapidly eroding Tsangpo Gorge region within the Yarlung-Siang-Brahmaputra River drainage (Figures 1a and 1b). It has been proposed that Quaternary glacial dams impeded bedrock river incision into the Tibetan plateau (Figure 1b; Korup & Montgomery, 2008; Korup et al., 2010) and that catastrophic glacial outburst megafloods focused erosion in the Tsangpo Gorge (Finnegan et al., 2008; Korup et al., 2010; Korup & Montgomery, 2008; Lang et al., 2013; Montgomery et al., 2004). Historical outburst floods caused by the failure of natural landslide dams have also been documented in the Gorge region (Delaney & Evans, 2015; Evans & Delaney, 2011; Shang et al., 2003; Zhu & Li,

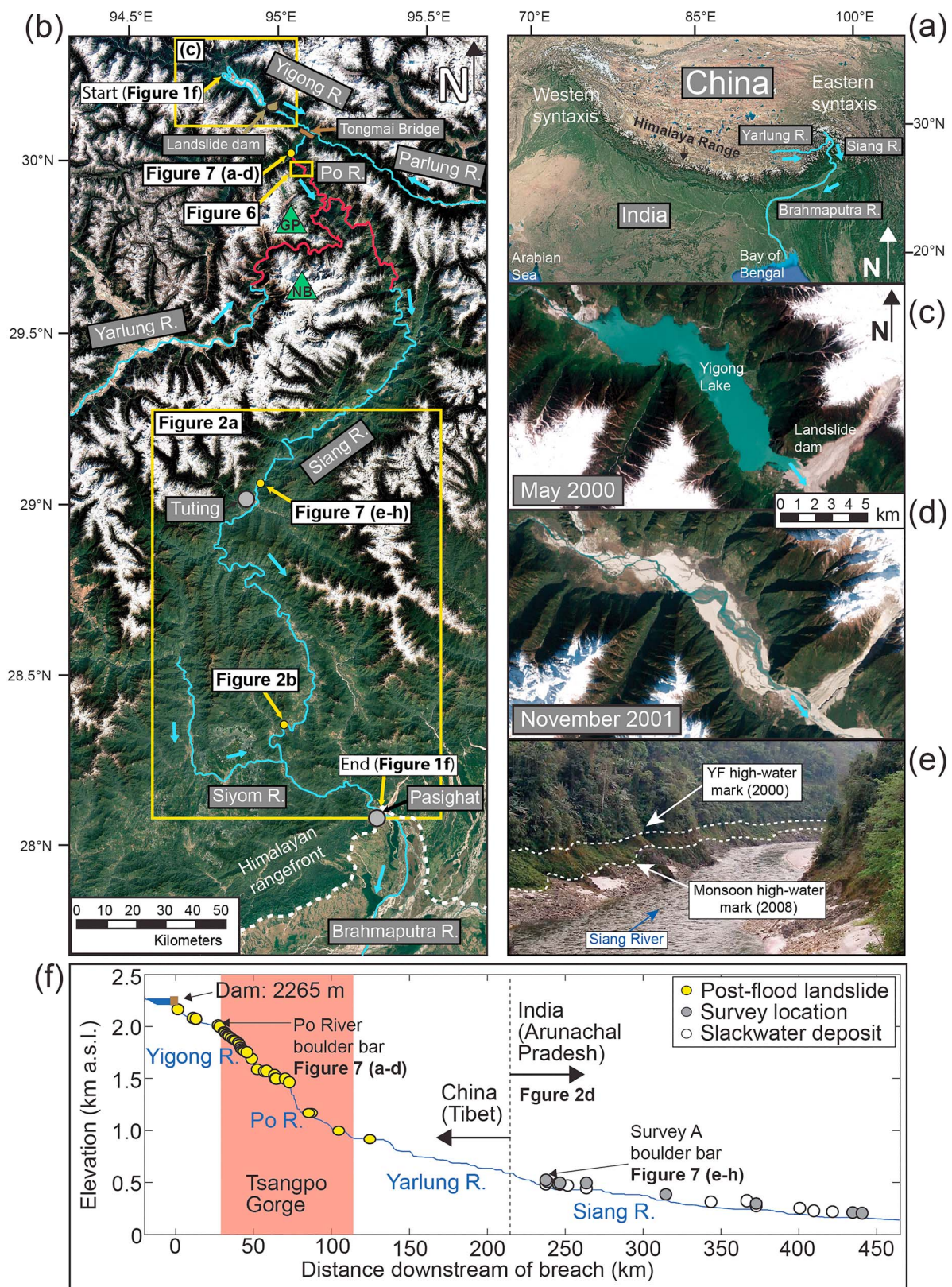


Figure 1. Google Earth image of the study area (a and b), with Tsangpo Gorge in red. The image in (b) shows the flood source, dam, and a close-up of the flood pathway. Landsat-7 imagery shows (c) the Yigong River impoundment and (d) the post-flood landscape. Photograph (e) shows mapped high-water marks of the year 2000 Yigong landslide-dam outburst flood (labeled YF) and the 2008 monsoon. The longitudinal river profile in (f) shows geomorphic features from the flood.

2000; Zhu et al., 2003). Such events have been linked both to lateral channel scour as a driver of landslide erosion (Larsen & Montgomery, 2012) and to sediment delivery effects on river transport capacity (Finnegan et al., 2008). These and other studies point to the potentially strong influence of outburst floods on the evolution of mountainous landscapes. Improved understanding of flood hydraulics should enable better understanding of the processes by which outburst floods erode and impact river morphology and the extent to which they might differ fundamentally from the processes at work during background flows.

This study examines the hydraulics and geomorphic effects of the second largest historical landslide-dam outburst flood on record, the June 2000 Yigong River outburst flood (Shang et al., 2003; Zhu & Li, 2000; Zhu et al., 2003). This flood coursed down a >450 km stretch of river through the rugged topography of the Tsangpo Gorge region before exiting the Himalayan range front (Figure 1). We numerically simulate the flood using the depth-averaged (two-dimensional, 2-D) shallow water equations for flow over three-dimensional topography. Well-balanced finite-volume methods and block-structured adaptive mesh refinement (AMR) are implemented in the open-source software GeoClaw (Berger et al., 2011; LeVeque et al., 2011) to enable efficient simulation of the advancing flood wave over the large ($>2.1 \times 10^4 \text{ km}^2$) spatial extent and multiday duration of the event. We compare simulation results to flood observations, discharge estimates, and new field-surveyed high-water marks and slackwater flood deposits to determine the applicability of the model for hazard assessment and geomorphic investigations in steep, rapidly incising landscapes. Spatial and temporal variations in flow depth, direction, and speed in the context of remote sensing observations enable us to investigate (1) spatial and temporal patterns of bed shear stress driven by the interaction of the flow with valley topography, (2) the size of blocks that can be plucked to incise bedrock, and (3) the potential effects of flood-related boulder bar formation on bed armoring and channel roughness relevant to long-term evolution of the Tsangpo Gorge.

2. Background

2.1. Geomorphic Setting and Outburst Floods of the Tsangpo Gorge Region

The eastern Himalaya is one of the most rapidly uplifting and eroding regions on Earth, characterized by extreme topographic relief and powerful rivers of the Yarlung-Siang-Brahmaputra River drainage (Figure 1a). Here, collision between India and Asia has produced mountains with >7 km peaks and long-term exhumation rates that exceed 5 km/Myr (Booth et al., 2009; Bracciali et al., 2016; Burg et al., 1998; Ding et al., 2001; Lang et al., 2016; Malloy, 2004; Seward & Burg, 2008; Zeitler et al., 2014). The Yarlung-Siang-Brahmaputra River slices through these high mountains of the Himalaya in Tibet and India, carving the Tsangpo Gorge in a knickzone where the river drops more than 2 km of elevation over a distance of <100 km. The river's high stream power and sediment transport capacity (Finnegan et al., 2008) through the Gorge have enabled it to cut a tortuous channel into bedrock between steep, rapidly eroding hillslopes at the threshold of failure (Larsen & Montgomery, 2012).

The high elevation, high relief, and rapid erosion set the stage for river damming and outburst floods. Sedimentary and geomorphic evidence from Tibet shows that outburst megafloods have occurred repeatedly over the last 50 ka, sourced from glacially impounded lakes in Tibet; failure of lakes as large as 835 Gm^3 unleashed peak discharges up to $5 \times 10^6 \text{ m}^3/\text{s}$ (Chen et al., 2016; Guangxiang & Xitao, 2007; Guangxiang & Qingli, 2012; Hu et al., 2018; Huang et al., 2014; Kaiser et al., 2010; Korup & Montgomery, 2008; Liu et al., 2015, 2006, 2018; Montgomery et al., 2004; Zhu et al., 2013, 2014). Historical outburst floods include those in 1900 and 2000 from landslide-dam impoundments on the Yigong River. These involved total flood volumes $>2 \text{ Gm}^3$ and peak discharge $>10^5 \text{ m}^3/\text{s}$ (e.g., Delaney & Evans, 2015). Both historic and Quaternary outburst floods are recorded by sedimentary deposits documented downstream of the Tsangpo Gorge along the Siang River (Lang et al., 2013).

The most recent and best recorded is the June 2000 Yigong flood (Evans & Delaney, 2011; Shang et al., 2003; Zhu & Li, 2000; Zhu et al., 2003). Delaney and Evans (2015) reconciled discrepancies among previous accounts of the dam, breach, and flood, summarized as follows: In April 2000, a rockslide dammed the Yigong River (Figures 1c and 1d) at the same location as the landslide-dam impoundment that produced the 1900 outburst flood (Shang et al., 2003). The landslide dam was stable for 62 days and a spillway was excavated before the dam failed catastrophically at ca. 21:30 on 10 June 2000 (Han, 2003; Shang et al.,

2003). The spillway had reduced the impounded lake elevation by 18 m (Yang et al., 2010), decreasing the flood volume released into the Yarlung-Siang-Brahmaputra River system by 1.0 Gm^3 . The $>2.0 \text{ Gm}^3$ flood was the second largest landslide-dam outburst flood in recorded history, second only to the Great Indus River flood in 1841 of about 6.5 Gm^3 (Evans & Delaney, 2011).

Dynamics of the 2000 Yigong flood (hereafter referred to as “the flood”) are constrained by limited direct observations and discharge estimates. At the breach, estimates of peak discharge based on empirical relations between impounded lake volume and discharge range from $6.1 \times 10^4 \text{ m}^3/\text{s}$ (Delaney & Evans, 2015, using the relation of Evans, 1986) to $1.3 \times 10^5 \text{ m}^3/\text{s}$ (Shang et al., 2003, using the relation of Costa & Schuster, 1988). Where the flood destroyed a highway bridge (Tongmai Bridge) 17 km downstream (Figures 1b and S1), peak discharge of $1.2 \times 10^5 \text{ m}^3/\text{s}$ was proposed by Shang et al. (2003; based on observations of peak stage) to have occurred 5 hr and 50 min after breach initiation; however, Delaney and Evans (2015) argue that peak discharge likely occurred much earlier given that the entire lake drained in ~6 hr (Zhu et al., 2003). Delaney and Evans (2015) simulated the first 50 km of the flood numerically using FLO-2D software and a 90-m digital elevation model (DEM). They initiated the simulation with a synthetic hydrograph scaled to their estimated peak breach discharge of $61,461 \text{ m}^3/\text{s}$, producing maximum discharge, water depth, and velocity estimates at Tongmai Bridge of $1.1 \times 10^5 \text{ m}^3/\text{s}$, 54.9 m, and 14.57 m/s, respectively (Figures 1b and S1). The initial flood wave was first recorded at a river gauge approximately 462 km downstream from the breach in the town of Pasighat, India, on 11 June at 18:00, an estimated 17 hr and 50 min after the breach initiated. Maximum rise in stage here was 5.54 m, and peak discharge was $4.4 \times 10^4 \text{ m}^3/\text{s}$ (four times the background discharge of $1.1 \times 10^4 \text{ m}^3/\text{s}$), measured 5 hr after the initial rise in the water level (Tewari, 2004). Tewari (2004) estimate that peak discharge at Pasighat occurred 22 hr and 50 min after the breach; the absolute time of flood arrival and peak discharge near Pasighat are known, but Tewari (2004) do not report the precise location of the Pasighat river gauge, and Evans and Delaney (2011) estimate an uncertainty in the breach timing of 30 min, which together contribute uncertainty to this travel time estimate.

The flood caused life and property losses, erosion, and sedimentation. In China it destroyed at least six bridges and damaged the highway system (Delaney & Evans, 2015). Many bridges were destroyed in Northern India, where the flood killed at least 94 people (Han, 2003). The flood also triggered significant landslide erosion (Larsen & Montgomery, 2012). No direct observations of bedload transport or channel incision are available. However, Lang et al. (2013) used an empirical estimate of peak breach discharge ($6.1 \times 10^4 \text{ m}^3/\text{s}$) and equations for bed shear stress and incipient motion to estimate that the flood could move blocks up to 3 m in size in the Tsangpo Gorge. The flood also produced alluviation along the Yigong River (Finnegan et al., 2008) and extensive slackwater sand deposits along the Siang River (Lang et al., 2013).

2.2. Numerical Simulation of Outburst Floods

Various numerical models have been used to implement the shallow-water equations in simulations of outburst flood inundation and dynamics for hazard assessment, infrastructure planning, and geomorphic studies (e.g., Cook & Merwade, 2009; Larsen & Lamb, 2016; Salvatore et al., 2013; Zin et al., 2018), but few models are well-suited to investigations of spatial and temporal variations in flow characteristics over large areas of rugged topography. One-dimensional models like HEC-RAS (U.S. Army Corps of Engineers) perform poorly when applied to rugged mountainous terrain (Alho & Aaltonen, 2008; Denlinger & O’Connell, 2009; Horritt & Bates, 2002) and are not useful for characterizing rapidly varying flow direction or lateral stresses along valley walls. Full three-dimensional modeling (using the Navier-Stokes equations with a free surface) might be necessary to capture the details of turbulent flows, but remains computationally infeasible for modeling the full extent of an outburst flood. Outburst flood simulation using 2-D models such as TELEMAT-2D (Galland et al., 1991), LISFLOOD-FP (Bates & De Roo, 2000), SOBEK (Carrivick, 2006), TUFLOW 2D (Alho et al., 2010), and ANUGA (Roberts et al., 2015) is feasible, and such models have been used successfully to study megaflood processes (Alho et al., 2010; Denlinger & O’Connell, 2009; Komatsu et al., 2009; Larsen & Lamb, 2016; Miyamoto et al., 2006).

However, even accounting for only two spatial dimensions, 2-D simulations that use a fixed computational grid (mesh) are computationally demanding—particularly when resolving flow characteristics at useful resolution (e.g., 30–250 m) over a large spatial domain. Simulations of outburst floods from Pleistocene

Glacial Lake Missoula, Montana, USA, required up to 250 days of CPU time for a complete flood simulation using a fixed grid with 250 m resolution (Denlinger & O'Connell, 2009). Recent simulations of Missoula floods achieved finer resolution (~30 m), but for a much smaller spatial extent in a limited area of interest and for short flow durations (<3 hr; Larsen & Lamb, 2016). Such fixed grids remain inefficient for a rugged mountain river over a large area because only a small proportion of the cells are inundated at a time.

For our analysis, we used GeoClaw, part of the open-source software package Clawpack (Clawpack Development Team, 2017; Mandli et al., 2016). GeoClaw incorporates a high-resolution wave-propagation algorithm to solve the depth-averaged 2-D shallow-water equations (equations 1–2 in the supporting information). A chief advantage of this model is that it uses an AMR, which clusters high-resolution rectangular computational cells in regions of interest along the flood pathway, automatically adjusting the region of refinement as the flow progresses (Berger et al., 2011; LeVeque et al., 2011). In this way, AMR enables efficient hydrodynamic simulation over large model domains. Similar to other models, outburst flood simulation in GeoClaw requires the user to define topography; dam location, height, and timing of dam removal; and roughness parameter, in addition to defining maximum grid resolution and setting the criterion for mesh and time-step refinement (described in section 3).

GeoClaw has been used extensively in tsunami modeling (e.g., Arcos & LeVeque, 2015; Macinnes et al., 2013) and has been formally validated for outburst floods with simulations of the Malpasset, France, 1959 dam-break flood (George, 2011). Recently, GeoClaw was used to simulate an ancient catastrophic glacial-lake drainage event in the Altai Mountains, central Asia, with the goal of linking flow characteristics to lake-bed sediment entrainment and bedform deposition (Bohorquez et al., 2015). Our study investigates a much larger magnitude outburst flood than the validation study of George (2011), and is the first to apply GeoClaw to simulate a modern landslide-dam outburst flood for which results can be compared to timing and maximum-stage observations of the flood for over >400 km downstream from the breach.

3. Methods

3.1. Field and Remote Sensing Surveys of Flood High-Water Marks, Slackwater Deposits, and Boulder Bars

We complemented sparse direct observations of flood hydraulics with field-surveyed high-water marks >200–400 km downstream of the breach along the Siang River. Flood inundation (trim line), indicated by the clear change from mixed vegetation in areas that were not inundated to rapid-growth vegetation (primarily banana trees) that colonized river banks scoured by the flood, was surveyed at eight locations (A–H; Figures 1 and 2 and Table S1). High-water marks were surveyed with a handheld GPS, laser range finder, clinometer, and/or tape measure in March 2008, before the start of the rainy season (March–September). At locations A–H we also surveyed the high-water mark of the monsoon river flow, indicated by the transition from bare bedrock to vegetated riverbank (Figures 1e and 2).

Twelve slackwater deposits from the flood were identified and sampled (Figures 1f, 2a, and 2d and Table S2) during field seasons in March 2008 and January 2013, four of which were reported previously by Lang et al. (2013). Flood slackwater deposits along the banks of the Siang River and its tributaries were unambiguously identified in the field based on their composition, sedimentary character and grain size, position on the landscape, level of vegetation, and lack of soil development, following the methods of Lang et al. (2013; Text S1 and Figure S2). All deposit positions were recorded with handheld GPS devices, and their elevations were derived from the DEM described in section 3.3 using the GPS positions. The vertical positions of seven of these deposits (#2–4, 7, 9–11) were also surveyed with respect to the river stage (near low flow at the time of all surveys) and monsoon high-water mark using a laser range finder and clinometer (Table S2). Some of these deposits (#1, 3, 4, 6, 9) were surveyed in locations where high-water marks were also identified and surveyed (locations A, B, C, D, and F) so that a direct comparison of relative elevation is possible. Grain size distributions for flood deposits were determined using a CamSizer L digital image processing particle and shape analyzer by Retsch Technology (Table S2).

Boulder bars were observed in the field and using Google Earth imagery from after the flood. We recorded the locations of all boulder bars that were resolvable on the imagery (i.e., >100-m-scale features) that were not associated with point bar deposition at the inside of meander bends. The location of the largest boulder

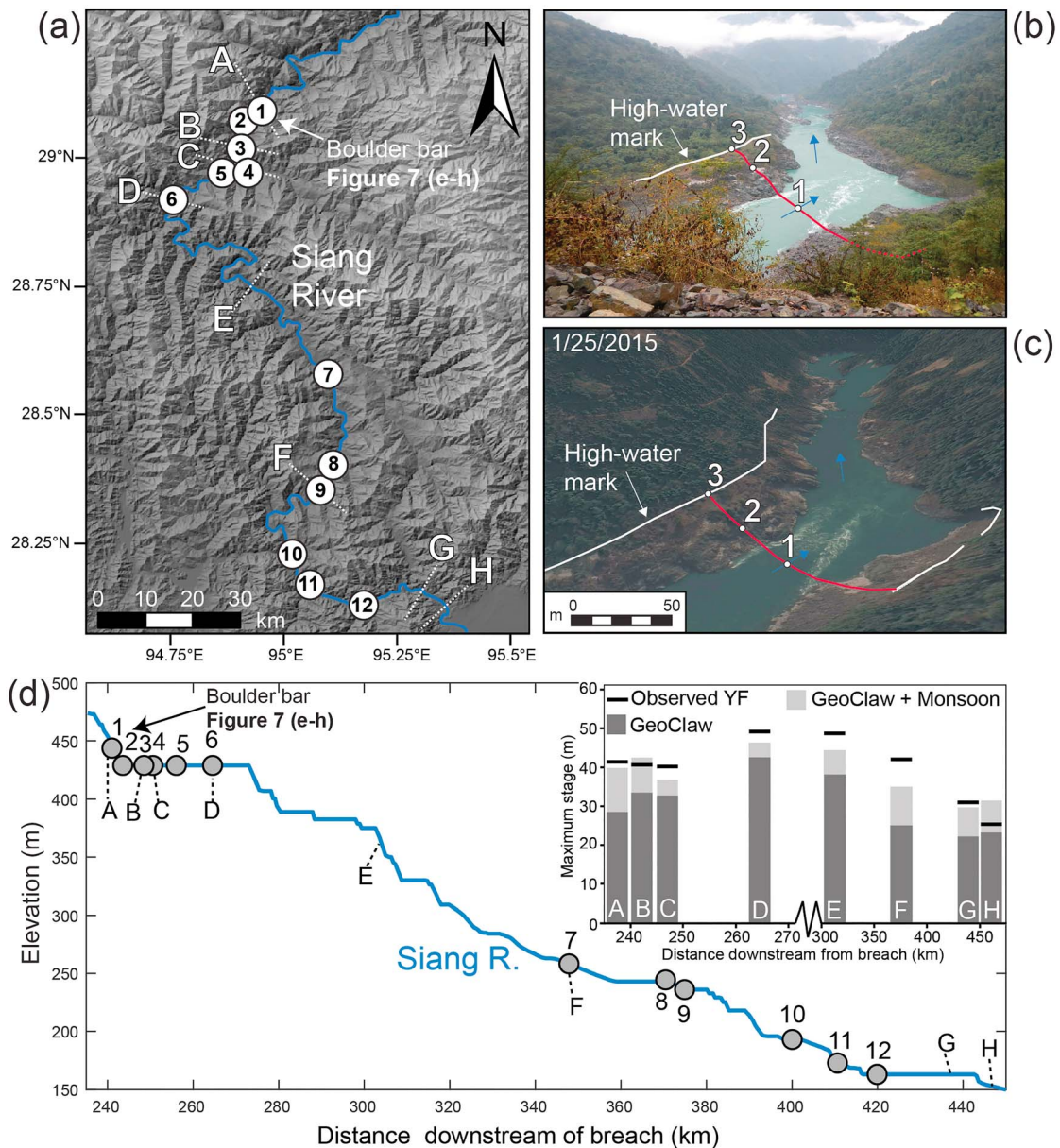


Figure 2. (a) Shaded digital elevation model shows locations of surveyed cross-sections with high-water marks A–H and observed slackwater deposits 1–12. Field photograph taken in January 2013 (b) and Google Earth image (c) downstream of survey C (28.3426°N, 94.9898°E) showing the low-flow water surface (1), monsoon stage (2), and flood high-water mark (3). (d) Longitudinal profile of the Siang River with survey stations and observed deposits; inset shows simulated and observed stage of the flood (labeled YF).

bar in the model domain (>1.5 km in length), which does occur near the inside of a meander bend, was also recorded. Particle size counts were conducted on two boulder bars, using Google Earth tools to measure intermediate axis lengths on all boulders that were well resolved in the imagery.

3.2. Numerical Simulations of the Flood Using Instantaneous Dam Failure

The flood was simulated in GeoClaw (version 5.4.1) on the basis of the landslide-dam height inferred by Delaney and Evans (2015) and assuming instantaneous dam failure at the breach. We modified the initialization routine in the GeoClaw code to replace the lake volume behind a landslide dam before the simulation begins; the dam was then instantaneously removed at the start of the simulation. The modified Python routine is available, along with the GeoClaw code and scripts used for flood simulation, on GitHub (see

supporting information). Our methods to develop the DEM, tune the desired AMR configuration and tune Manning's roughness coefficient, n , are summarized below. User-controlled variables in the run-file include parameters to adjust time steps, solver method, boundary conditions, and physical variables like gravity and are listed in Table S3 (see documentation on GeoClaw website: Clawpack Development Team, 2017).

3.3. Topographic Data and GeoClaw AMR

The flood was simulated on a DEM spanning 21,554 km². The DEM is a combination of two data sources: the SRTM 3 arc-second (~90 m cells) DEM with voids filled using topographic contour data (de Ferranti, 2014), and a higher-resolution SRTM 1 arc-second (~30 m cells) DEM (SRTM data acquired February 2000). The 30 m SRTM1 data set is used in the Yigong River and Po River reaches encompassing the first 47 km of the flood pathway (distance measured along the middle of the channel downstream of the dam breach), and in the Siang River from ~124 to 465 km along the pathway. The 90 m SRTM3 data set is used for the 77 km between these two segments (5.7% of the total area of the SRTM1 DEM) because of poor coverage by the 30-m SRTM1 data set in this area. All geomorphic observations and analyses were made in the area covered by the higher-resolution SRTM1 data set. Flood simulations (1) assume that the topographic boundary for the flood is the water surface (and valley walls) from SRTM1 data acquired prior to the flood in February 2000, not the actual channel bed, and (2) ignore any topographic changes that may have occurred during the course of the flood.

The AMR capability in GeoClaw efficiently simulates the flood by adaptively concentrating computational grid cells in a narrow band where water is present around the channel. A coarse level-1 rectangular grid with resolution of ~1 km covers the entire computational domain, a rectangle of size 86 × 244 km or nearly 2.1 × 10⁴ km². Four more levels of refinement are used for the flood simulation that refine in space and time by successive factors of 4, 2, 2, and 2, respectively, so that level-5 has 30 m resolution. The time steps on each level are varied based on the Courant-Friedrichs-Lewy condition (Berger et al., 2011). Initially, we force level-4 grid patches (60 m resolution) covering the region around the impounded lake. As water begins to flow into the channel following the breach, higher levels of refinement are automatically applied only around the flowing water. Different criteria can be used to flag cells for refinement, but the default AMR criterion based on water depth was used for these simulations, ensuring that almost all of the flow is simulated at the highest level of AMR (level-5; 30 m cells). By regridding every few time steps it is possible to automatically expand the portion of the valley that is refined as the flood progresses and resolve the wet-dry boundary of the flow through time on the DEM.

For the simulations reported here, we set the refinement criteria to ensure that the majority of flow computations are performed on the highest-level grid (level-5), which corresponds to a maximum grid resolution of 30 m. The 30-m grid resolution matches the resolution of our DEM except in the middle of the flood pathway where the resolution is 90 m. In order to perform 30-m grid resolution simulations in the areas covered by the 90-m DEM, the software constructs a piecewise bilinear surface that is then integrated over each finite volume grid cell to determine the average topography value used in that cell. Using this method it is possible to simulate the flow at extremely high-resolution (e.g., <5 m) AMR levels even on relatively coarse topographic data. We focus on examining 30-m-resolution simulated hydraulics in areas where we use the SRTM1 30-m DEM, so that the highest level of the simulated topographic surface matches the resolution of the DEM. Additional simulations, reported in the supporting information, were performed to test the sensitivity of the computed solution to the grid resolution with maximum grid resolutions that range from 15 to 60 m.

3.4. Selection of Spatially and Temporally Uniform Manning's Roughness Parameter, n

Manning's roughness parameter (n) in the friction term of the shallow-water equations (supporting information, equation 2) was 0.04 for most simulations presented in the main text of this paper, but we also compared results from simulations using $n = 0.02$ and $n = 0.06$ (see supporting information). For all simulations, n is spatially uniform and does not vary with time, following previous outburst flood studies (e.g., Alho et al., 2010; Bohorquez et al., 2015; Clarke et al., 2004; Denlinger & O'Connell, 2009; Miyamoto et al., 2006; O'Connor & Baker, 1992; O'Connor, 1993).

The range of n values applied here is similar to the ranges tested in previous 1-D and 2-D simulations of ancient megafloods ($n = 0.025$ to 0.075), for which simulated discharges varied minimally as a function of the roughness parameter (Carling et al., 2010). The GeoClaw outburst flood simulations of Bohorquez et al. (2015) used $n = 0.05$ based on a gravel grain size reference value of 0.035 m consistent with Carling (1996a, 1996b). Several other megaflood modeling studies estimated the bed roughness scale, k_s , to calculate n with the Manning equation (Henderson, 1966; Manning, 1891). For example, researchers simulating Missoula floods characterized the average height of the surface roughness in the full domain of the model (0.17 – 0.81 m) and used these values and the Manning equation to calculate a range of $n = 0.031$ – 0.04 (Denlinger & O'Connell, 2009). Denlinger and O'Connell (2009) chose the $n = 0.031$ value for flood simulations, which is close to the value used in similar bedrock channels ($n = 0.038$) for flood simulation in the Verde River, Arizona, USA (Denlinger et al., 2002). More recent simulations of Missoula floods have estimated k_s using a model in which n scales with the standard deviation of bedrock elevations of the channel (Larsen & Lamb, 2016), producing an n value of 0.065 that is higher than the values used in most other flood simulations.

Channel roughness likely varies in different segments of the flood pathway on the Yigong, Po, and Siang River. For instance, we expect higher natural roughness ($n = 0.06$) along the Po River (Tsangpo Gorge) because of the rugged channel morphology and large roughness elements, including boulders locally larger than 10 m. Sediment input from numerous landslides here may also lead to higher roughness during the flood. Further downstream (>200 – 400 km) in the Siang River, exposed bedrock in the valley is smoother and channel roughness elements are generally smaller than in the Po River, suggesting a lower value ($n = 0.02$). We discuss results of $n = 0.02$ – 0.06 simulations, but focus on simulations with spatially uniform $n = 0.04$ that is more typical of most previous flood modeling studies. Equating the Manning-Strickler relation and Manning equation, and using an estimated bed roughness length-scale, k_s , of 1 m, we calculate a value of $n = 0.039$, further supporting our choice of $n = 0.04$ for simulations (see supporting information).

4. Results

4.1. Observations of Flood High-Water Marks, Slackwater, and Boulder Deposits

The positions of 12 slackwater deposits and 8 high-water marks from the Yigong flood are shown on the river profiles in Figures 1f and 2d. Additional information about the deposits is in Table S2. Observed median grain sizes (D_{50}) in the range of 0.115 – 0.355 mm confirm the deposits are very-fine to medium sand (Table S2). High-water marks mapped in the field range from 22 to 48 m above the low-flow water surface at the time of the survey. These flood stages are on the order of 13 – 36 m above the typical annual monsoon high-water level (Table S1). Monsoon stage at these locations ranges from 8 to 14 m and averages 12 m above low flow (Table S1). Flood stage measured with respect to the monsoon high-water mark is the most relevant measurement of the rise in flood stage because the flood occurred in June, when hydrographs along the Siang River typically begin to reach monsoon levels (Datta & Singh, 2004).

A total of 76 greater-than-100-m-scale boulder bars that were not located at the inside of meander bends were mapped along the flood pathway; their locations, as well as that of the largest boulder bar in the model domain, which does occur near the inside of a meander bend, are presented in the supporting information (BoulderBar.kmz). Sixty-nine of the mapped boulder bars are within 320 km of the breach; downstream of this point, boulder bars are less frequent. Particle size counts for the largest boulder bar, located 26 km downstream of the breach in the steepest part of the flood pathway on the Po River, and for a characteristic non-point-bar boulder bar on the Siang River near survey location A and deposit 1 are also reported (Table S4). The median intermediate axis length on the largest Po River boulder bar and Siang River boulder bar near location A are 5 and 3 m, respectively. Grain size decreases downstream and intermediate axis length becomes difficult to resolve with Google Earth imagery for the eight bars located >320 km downstream of the breach.

4.2. Simulations of Flood Hydraulics

Results from the full range of simulated grid resolutions and roughness values are reported in the supporting information, including animations of model output from $n = 0.04$ simulations showing flow depth, calculated shear stress, and Froude number (Figures S3 and S4; Tables S5, S6, and S7; and Movies S1–S8).

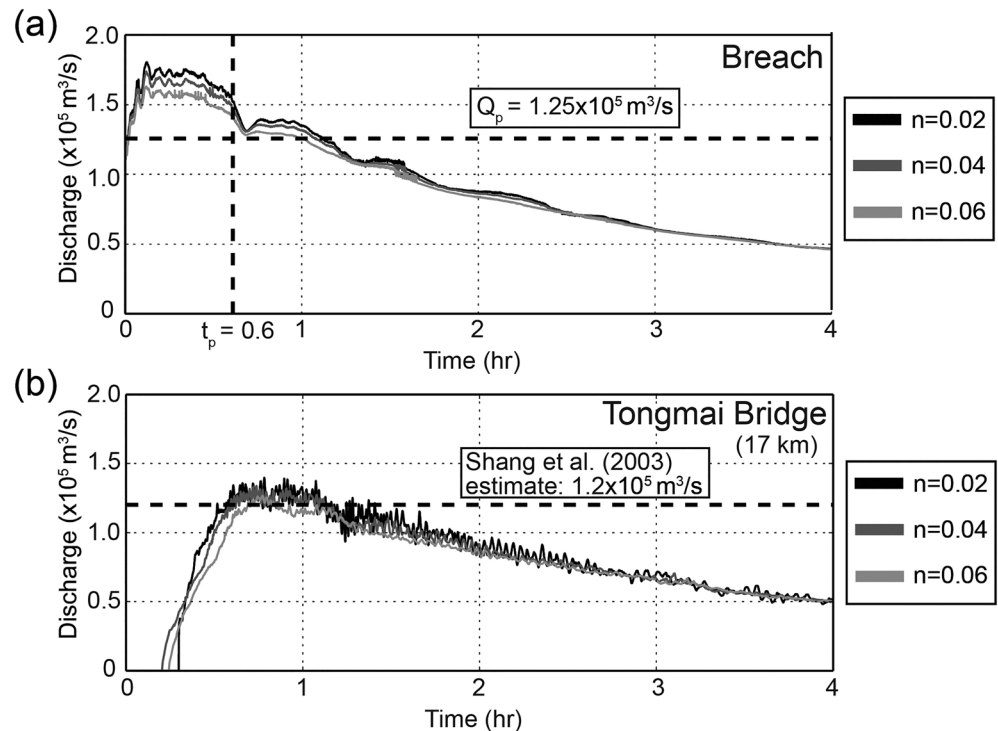


Figure 3. (a) Discharge recorded at the breach from simulations with $n = 0.02, 0.04,$ and 0.06 over the first 4 hr of the flood. Q_p is the estimated peak discharge using predictive equations from Walder and O'Connor (1997), and t_p is the time of peak discharge estimated using a rapid natural landslide-dam failure rate. (b) Hydrographs from the same simulations at Tongmai Bridge that show little sensitivity to n .

Simulations with maximum grid resolution of 15 m encountered instabilities in flat-lying areas of topography generated from the SRTM1 30-m data set that made it difficult to accurately map inundation. Therefore, we restrict discussion here to a summary of results of 30-, 45-, and 60-m simulations.

Near the breach, simulated flow depths (stages) are relatively insensitive to the choice of grid resolution and n . For simulations with 30-m maximum grid resolution and $n = 0.04$, the peak breach discharge ($1.73 \times 10^5 \text{ m}^3/\text{s}$) occurred 0.12 hr after the breach (Figure 3a). The peak breach discharge and arrival time in the $n = 0.02$ and 0.06 simulations differ from these values by up to 3.7% and 6.2%, respectively (Table S6). At 17 km downstream of the breach at Tongmai Bridge, the shapes of simulated hydrographs are nearly identical for $n = 0.02, 0.04,$ and 0.06 simulations; the time of flood wave arrival for these roughness values ranges from 12 to 24 min (Figure 3b and Table S6). Simulations using $n = 0.02$ and grid-resolutions of 30–60 m also produce similar hydrographs, with peak discharge on the order of $1.39 \times 10^5 \text{ m}^3/\text{s}$ (Figure S3). Simulated maximum flow depths at this location range from 76 to 79 m (i.e., <4% difference) using various combinations of n and grid resolution and occur at 1.2–1.7 hr after the breach (Table S6).

Maximum flow depth and speed vary spatially along the flood pathway as a function of valley shape (e.g., Figures S4 and S5). For all n and grid-resolution simulations, the highest flow depths (up to 108 m) and speeds (up to 56 m/s) are observed 28–49 km downstream of the breach along the Po River (Figure S5). Here and at other locations, maximum flow depths are higher (and velocities lower) above valley constrictions than immediately downstream (Figures 4 and S5). At the high-water mark survey and deposit locations, maximum flood stage ranged from 21 to 41 m above the base of the DEM for the 30-m resolution, $n = 0.04$ simulations (Tables S1 and S2).

Although spatial patterns of flow speed are relatively insensitive to n , the magnitude of flow speed varies substantially with n , affecting local flow velocity and downstream flood translation. As a result, the timing of flood wave arrival is increasingly sensitive to the choice of roughness parameter with distance downstream (Table S6). At location A, 238 km downstream of the breach, arrival time for the 30-m grid resolution simulations varies by up to 15% (1.9 hr) between $n = 0.02$ and 0.06 simulations (Figure S4 and Table S6). At

the farthest extent of the flood simulation 462 km downstream of the breach, the timing of the flood wave arrival varies by 25% (25.3 to 31.7 hr) for 30-m simulations with different n values (Table S6). Simulated flood travel times from the breach to Pasighat for the $n = 0.02$ and $n = 0.04$ simulations are $\sim 10\%$ and 25% greater than the travel time reported by Tewari (2004), respectively.

Simulated flow depths at deposit and survey locations up to 373 km downstream of the breach (locations A–F) are relatively insensitive to the choice of roughness parameter (Figure S4), but flow depths between different n simulations vary by up to a factor of two further downstream where the valley is wider. Maximum simulated flow depths for 30-m simulations vary by only 1–7% (0.4 to 1.7 m) as a function of roughness parameter at locations A–F. In the distal part of the flood simulation, 435–440 km downstream of the breach at locations G and H, maximum flow depths vary by 78.5% (16.3 m) and 102% (22.6 m) between the $n = 0.02$ and $n = 0.06$ simulations, respectively (Table S6).

5. Evaluation of Flood Simulation Results

Here we compare simulations and observations of the flood to evaluate the major assumptions in our modeling approach, including instantaneous dam failure and topographic boundary conditions.

5.1. Sensitivity of Model Results to the Assumption of Instantaneous Dam Failure

The assumption of instantaneous dam failure in our simulations leads to higher peak discharges and shorter time to peak discharge than would be expected based on empirical estimates for dam failure (O'Connor & Beebe, 2009). At the breach, simulated peak discharge ($1.73 \times 10^5 \text{ m}^3/\text{s}$) exceeds by 32% the discharge ($1.25 \times 10^5 \text{ m}^3/\text{s}$) estimated using the benchmark predictive equations for natural, constructed, and scale-model dam failures of O'Connor and Beebe (2009) and Walder and O'Connor (1997; Figure 3a). More information about the geometry of the Yigong landslide dam would be needed to apply breaching models using sophisticated predictive equations that involve dam dimensions (e.g., Froehlich, 2016). The time to peak discharge, t_p , can be estimated based on the timescale of natural landslide dam failures, which varies over several orders of magnitude depending on the erodability of landslide material and failure mechanism (e.g., Garcia-Castellanos & O'Connor, 2018; O'Connor & Beebe, 2009; Walder & O'Connor, 1997). Many natural landslide dams made of unconsolidated material fail by overtopping in <1 hr (Canuti et al., 1994; Costa, 1988; Costa & Schuster, 1991; Hewitt, 1968; King et al., 1989; Plaza-Nieto & Zevallos, 1990), but dam erosion rates can also be several orders of magnitude slower, thereby producing longer breaching timescales (e.g., O'Connor & Beebe, 2009, and references therein). The unconsolidated Yigong landslide dam failed by overtopping, so we expect a rapid time to peak discharge, potentially on the order of $t_p = 0.6$ hr based on the erosion rate of the natural dam on the Birehi Ganga River in India ($2.5 \times 10^{-2} \text{ m/s}$; Figure 3a; O'Connor & Beebe, 2009). Given the variability in flow speed from simulations with different roughness values (Figure 3a), t_p on the order of 1 hr or less suggests that the precise timescale of dam failure may have less effect on the timing of flood wave arrival downstream than the magnitude and spatial variability of natural roughness.

At Tongmai Bridge 17 km downstream, our instantaneous dam-breach simulations yield peak discharge and flow depths that are higher than previous model results, but similar to estimates based on field observations of stage. Our simulated maximum discharge and flow depth (76 m) are higher than the $1.1 \times 10^5 \text{ m}^3/\text{s}$ discharge and 54.9 m flow depth estimates produced by the FLO-2D simulations of Delaney and Evans (2015). Much of this difference likely results from the use of an empirically estimated breach discharge ($6.1 \times 10^4 \text{ m}^3/\text{s}$) in the Delaney and Evans (2015) model, which is much lower than the discharge produced by both our simulations assuming instantaneous dam failure and predictive equations for dam breaching from O'Connor and Beebe (2009). However, it is difficult to compare the simulations directly because Delaney and Evans (2015) simulated the flood using an older DEM (SRTM3) that differs from our DEM (SRTM1) in the first 20 km of flood pathway. It is also difficult to compare simulated flow depth and flood peak arrival time to the field-based estimates of Shang et al. (2003) because of uncertainties in the reference point for measuring flood flow depth with respect to the destroyed bridge height as compared to the simulated flow depth with respect to the DEM surface and the potential incompatibility of the Shang et al. (2003) timing estimate with other observations of the flood (Zhu et al., 2003). Nevertheless, our simulated

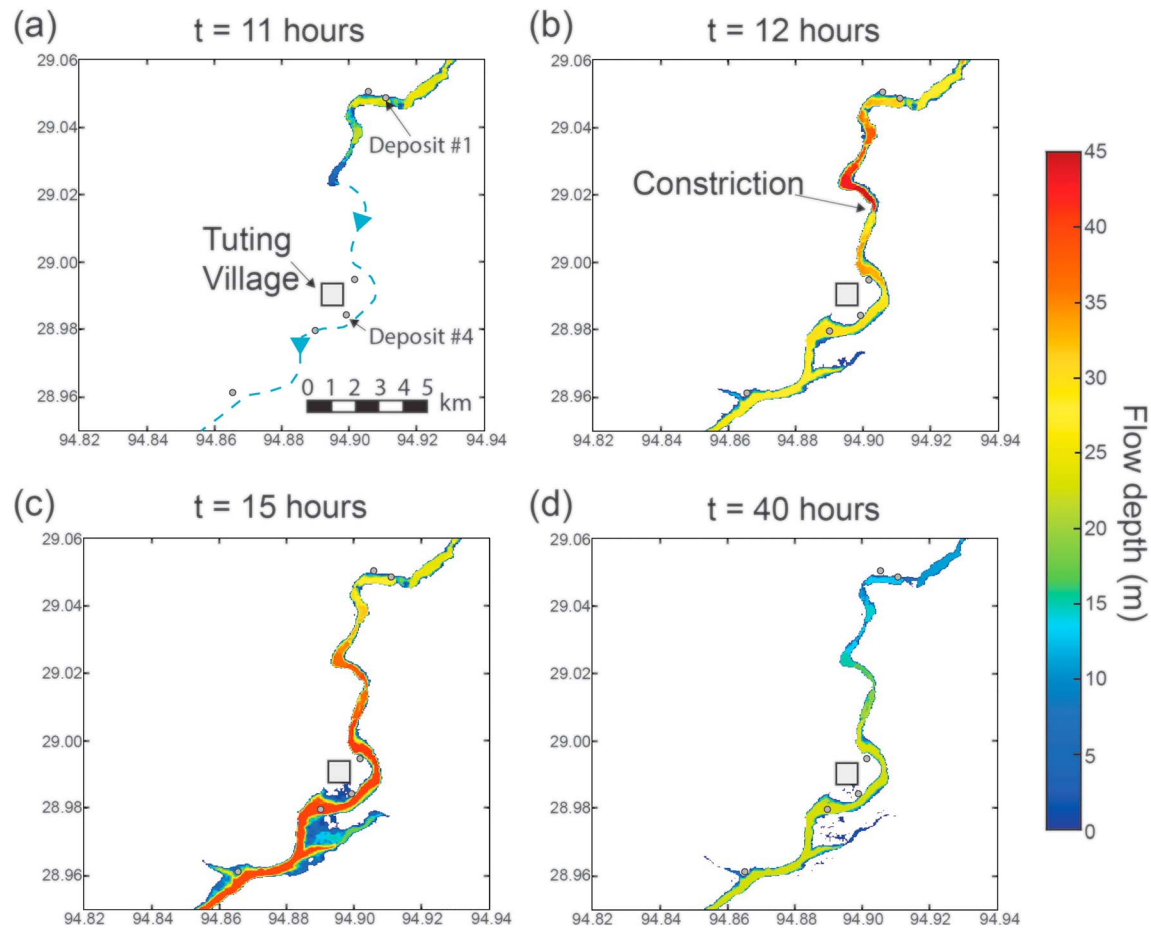


Figure 4. Simulated depths for $n = 0.04$ simulations around the Tuting village. (a) The flood wave arrives around ~ 11 hr after the breach. (b) Flow depths up to 45 m occur behind a valley constriction at $t = 12$ hr. (c) Maximum inundation occurs at $t = 15$ hr. (d) Flow depths at $t = 40$ hr after the breach, by which point flood waters have receded from terraces where slackwater sand deposits were observed; see Movies S1–S8 for additional time steps.

peak discharge only exceeds the maximum instantaneous discharge at Tongmai Bridge reported by Shang et al. (2003) by $\sim 10\%$, which indicates good agreement given the uncertainties.

5.2. Comparison of Simulated Stage to Observed High-Water Markers and Deposits

We focus on high-water marks mapped in the field as the most robust data available to evaluate simulated flood stages (Figures 1e and 2 and Table S1). Some apparent scour features are visible in post-flood Landsat-7 imagery of the first 20 km of the flood (Figure S1), but the available cloud-free Landsat 7 scenes immediately postdating the flood (June 2000) do not permit high-water marks to be unambiguously distinguished from slumping and mass failures near the edge of the channel. Clearer imagery was acquired too long after the flood (26 months) to precisely constrain flood-coeval bank erosion as a proxy for maximum inundation.

Simulated inundation should exceed the elevation of all deposits (Table S2) and meet all mapped high-water marks (locations A–H; Table S1). Simulated stages exceed the level of 9 of the 12 deposits reported in Table S2, and of the high-water mark at location H, but do not attain the level of high-water marks along the Siang River at field survey locations A–G (Table S1). The mismatch generally increases downstream, ranging from 15–22% of observed flood stage at A–C (238–247 km downstream of the breach) to 27–37% at D–G (264–435 km downstream of the breach; Table S1). High-water mark elevations were surveyed with respect to the river low flow level with submeter-scale accuracy; additional error in the relative position of these measurements with respect to the simulation owes to uncertain interpretation of maximum flood stage due to vegetation growth since the flood, which we estimate to be on the order of 0.5 m, and also to uncertainties in the DEM itself. The magnitude of the discrepancies indicates that measurement error alone cannot

explain these results at most locations. The mismatch cannot be explained by instantaneous dam failure, which results in flow depth overestimates rather than underestimates.

The flood occurred during monsoon flow conditions, but we do not explicitly model monsoon discharge; therefore, some of the discrepancy between simulated and observed stage may arise because the DEM representing the position of the water surface and valley walls is based on elevation data acquired at low flow. Ideally, we would test this hypothesis by comparing discharges from the flood simulations to estimates of monsoon and flood discharges at each survey location. Discharge (Q) can be estimated as the product of the flow cross-sectional area (A) and velocity (V) estimated from Manning's equation:

$$V = \frac{1}{n} \left(\frac{A}{P} \right)^{\frac{2}{3}} S^{\frac{1}{2}}, \quad (1)$$

where P is the wetted perimeter and S is the channel gradient, which is assumed to be the water surface slope. Our field measurements of monsoon and flood high-water marks combined with DEM measurements should in theory enable monsoon and flood discharges to be calculated in this way. However, the coarse resolution of the DEM introduces large uncertainties in channel gradient measurements, particularly in Siang River segment of the flood pathway where $S < 0.002$. Measurements of A are underestimated based on the DEM due to the lack of bathymetric data for the channel. The choice of n also contributes to uncertainty in velocity and therefore discharge estimates. We suggest such uncertainties make it difficult to estimate discharges within ~50–71% (Text S6), making the calculation of limited use for our analysis.

We therefore evaluate the hypothesis that the addition of monsoon flow could account for the discrepancy between simulated and observed flood stages using rough estimates of the amount of water displaced by the monsoon that is not accounted for in the model. Calculating the cross-sectional area of water displaced by the monsoon taking into account valley geometry at all field survey stations (Figures 5, S6, and S7) produces stage adjustments of 1–5 m (2–12% of flow depth) for survey locations A–G (Figure 2d). At survey H (440 km), simulated stage exceeds the observed high-water mark (Figure S7) so that the adjustment here is an overestimate of 7 m or 31% of the observed flow depth, which is potentially due to variations in natural roughness that are not accounted for in the model.

We suggest adjustments of this scale would be sufficient to raise flow depths above the three deposits (#2, 8, and 10) that were not inundated in our simulations. Simulated flow depth falls short of inundating deposit #10 by <1 m and #2 by only 1 m (3% of flow depth), while deposit #8 is 3 m (13% of flow depth) above the maximum simulated flow depth (Table S2). Some of the difference at deposit #8 may owe to position uncertainties of 7–15 m from the hand-held GPS, resulting in elevation uncertainties of at least 7–15 m compared to the flow depth in these locations.

Although the area-based approach does not explicitly account for discharge, the above calculations nevertheless suggest that the discrepancy between observed and simulated stages may be approximately accounted for by adjusting river base level for monsoon stage at the time of the flood. The magnitude of simulated-observed stage mismatch generally increases downstream (Table S1), as does total monsoon discharge, suggesting that geomorphic analyses may be most robust in the first ~250 km of the flood pathway. At the farthest downstream point of our simulation in Pasighat, observed monsoon discharge is on the order of $1.1 \times 10^4 \text{ m}^3/\text{s}$, or 25% of the total peak discharge during the flood (Tewari, 2004). Future work will explicitly simulate monsoon discharge calibrated to these observations in order to rigorously assess the contribution of background discharges to flood stage and hydraulics.

The choice of uniform roughness parameter also likely contributes to the mismatch between observed and simulated stages. The fact that $n = 0.04$ models overestimate the travel time of the flood wave from the breach to Pasighat reported by Tewari (2004) is consistent with our expectation based on the scale of roughness elements observed in the field that a lower roughness value may be more appropriate for the distal portions of the model domain. Failure to account for such spatial (as well as temporal) variations in roughness may also contribute to the divergence of simulated and observed stages in distal portions of the flood pathway, particularly where wider channel/valley morphologies (e.g., Figure S7) may contribute to increased sensitivity of the flow to local bed roughness.

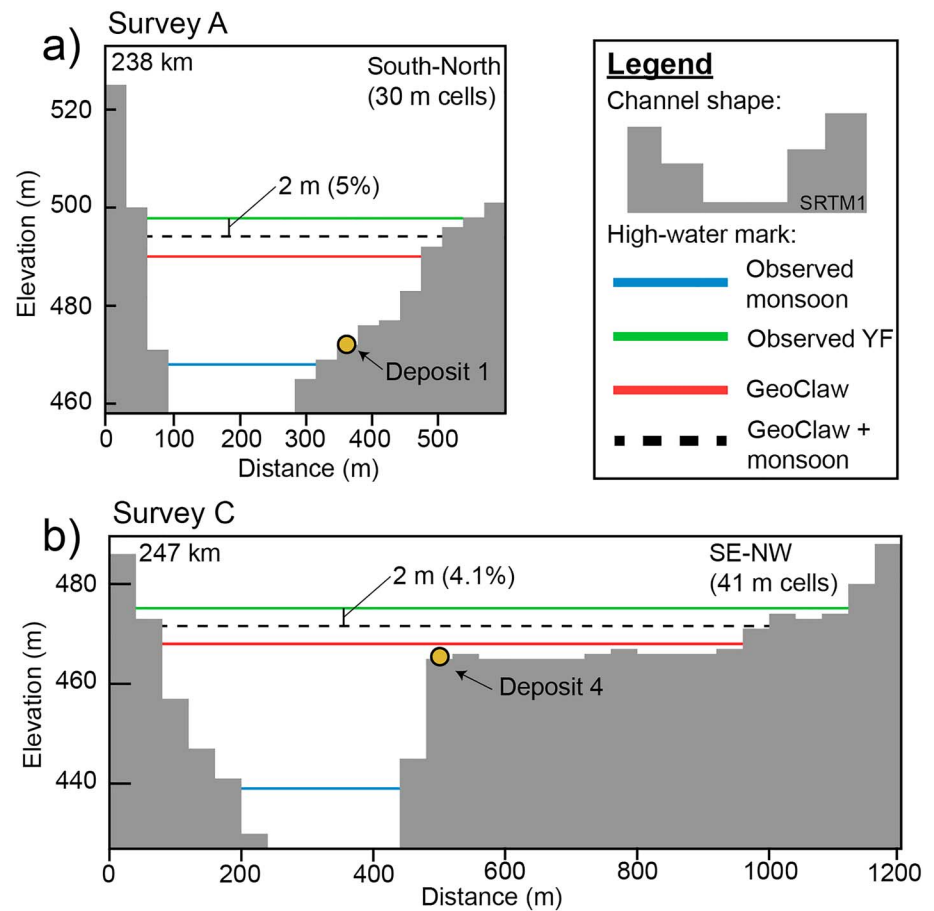


Figure 5. Simulated stage mapped onto valley topography represented by the SRTM1 DEM at survey locations A (a) and C (b). The observed monsoon (blue) and flood high-water marks (green) were mapped with respect to the lowest elevation in the DEM cross-section. The dotted line represents the sum of the cross-sectional area of the monsoon and GeoClaw simulation at each location. The cross-sections are oriented downstream and the width of the cells depends on the trend of the cross-section with respect to the DEM. See supporting information for additional plots and details. DEM = digital elevation model.

6. Insights Into Outburst Flood Hazard and Geomorphic Processes From Flood Simulations

The modeling results match field evidence to the extent that we judge the simulated hydraulics to be relevant to flood hazard and geomorphic investigations, despite the assumption of instantaneous dam failure, use of spatially and temporally uniform roughness parameter, and lack of explicitly modeled monsoon river base flow. We therefore consider simulated hydraulics in the context of flood hazard assessment and of valley morphology, erosional features, and deposits. Computation is efficient and inundation patterns are relatively insensitive to grid resolution and roughness parameter at the scale of the 30-m DEM, making this a promising modeling approach for hazard assessment in mountainous regions. Flow depth, speed, and direction, as well as the magnitude, duration, and spatial distribution of calculated bed shear stress, are strongly influenced by the interaction of the flow through complex valley topography above the modern channel—with implications for fluvial and hillslope erosion and for sediment transport and deposition in outburst floods.

6.1. Implications for Flood Hazard Assessment in Mountainous Topography

Hazard from landslide-dam outburst floods is well known in mountainous landscapes around the world, many of which experience frequent earthquakes that make them especially prone to landslide-damming and subsequent failure (e.g., Korup, 2002, 2005; O'Connor & Beebe, 2009; O'Connor et al., 2013; Ruiz-

Villanueva et al., 2017; Weidinger, 2006; Xu et al., 2009). There is also a growing risk of glacial-outburst floods in the Himalaya and other orogens as glaciers respond to modern climate change and produce moraine-dammed supraglacial and proglacial lake systems (Westoby et al., 2014; Worni et al., 2013). Although typically smaller than the Yigong flood, modern glacial-outburst floods can be just as deadly and damaging to infrastructure (e.g., Richardson & Reynolds, 2000). Significant hazard is also associated with ongoing and planned hydropower projects around the Himalaya and other mountainous regions (e.g., Ahlers et al., 2014; Sattar et al., 2018; Schwanghart et al., 2016, 2018).

Outburst flood simulation can be a cost-effective tool for hazard assessment and mitigation planning in mountainous terrain (e.g., Allen et al., 2016; Bajracharya et al., 2007; Frey et al., 2018; Kougkoulos et al., 2018; Schneider et al., 2014; Shrestha et al., 2010; Wang et al., 2018). However, most such modeling has been limited to relatively small events (but c.f., Risley et al., 2006). We have illustrated that GeoClaw enables modeling at a scale and resolution not previously possible, efficiently computing hydraulics along a >400-km-long stretch of a complex river channel with an effective resolution of 30 m. Our results provide evidence that the shallow water equations, together with the GeoClaw implementation, can be used for such studies to produce results that compare well with observations. This work supplements earlier validation studies for smaller outburst floods based on simulations of the Malpasset, France, 1959 dam-break flood (George, 2011).

In particular, we have shown that the inundation patterns of the simulation results compare reasonably with observed high-water marks when a basic adjustment for monsoon baseflow is taken into account (Figure 2d), despite inherent uncertainties in the modeling due to the lack of high-resolution topographic data and lack of knowledge of the (spatially varying) surface roughness. Another source of uncertainty is the dam failure mechanism and timing. The assumption of instantaneous dam failure, such as we have made here, may be appropriate for examining flood hazard and hydraulics downstream because it represents a worse-case scenario of breaching and provides maximum estimates for peak discharge and flow depth downstream. However, this treatment of the dam failure could be improved with more sophisticated empirical dam breaching models (e.g., Froehlich, 2016; Westoby et al., 2015), particularly if parameters related to the geometry and composition of the dam are known. The precise timescale of the Yigong dam failure is unclear (Delaney & Evans, 2015; Shang et al., 2003; Zhu et al., 2003) and likely <1 hr, but future simulations could investigate the effects of different breaching rates and dam parameters on downstream flow conditions.

Comparison of GeoClaw results to observations further downstream in populated areas of the Siang River valley suggests that accounting for monsoon baseflow in the drainage may be more important to flood modeling and hazard assessment in this region than the addition of a more sophisticated dam removal scheme. Simulated flow depths that are uncorrected for monsoon stage consistently underpredict observed high-water marks in the distal portion of the flood path (Figure 2d and Table S1). We expect that simulations that explicitly model baseflow on a higher-resolution DEM will produce more detailed inundation patterns that are needed to accurately map flood hazard. The previous GeoClaw modeling study of the Malpasset flood achieved simulation of stage within meters of field observations on topographic data with up to 2 m sized cells (George, 2011). Although DEMs up to 8 m in resolution are now available in some parts of the Himalaya (Shean, 2017), these data do not cover the Tsangpo Gorge or more populated areas like Tuting village. More coverage of this 8 m data set would be useful to assess hazard from different flood scenarios in the area by enabling better resolution of channel boundaries and the shape of floodplains, which is required for more accurate inundation predictions around low-relief populated areas of the Siang River valley.

Not only the inundation pattern, but also the timing of flood wave arrival is important for planning evacuations of populated areas before a future outburst flood event that is imminent. Our simulated flow depths are relatively insensitive to the choice of roughness parameter up to 373 km downstream of the breach (Table S1), but the flow speed and flood wave arrival timing vary significantly as a function of n (Table S6). Spatially variable, and potentially temporally variable roughness in the model, along with a more sophisticated dam failure scheme, may be necessary to accurately predict the timing of inundation. Uncertainties in the observations of the event timing make it difficult to discriminate the relative importance of these simplifications for the accuracy of flood timing prediction. Nevertheless, simulations with instantaneous dam failure and low roughness ($n = 0.02$) offer timing estimates that could be considered a worst-case scenario (i.e., fast downstream translation) useful for hazard assessment.

6.2. Outburst Flood Hydraulics, Shear Stress Patterns, and Implications for Erosion

Outburst floods can cause significant block plucking and channel incision in jointed bedrock (e.g., Lamb & Fonstad, 2010; Larsen & Lamb, 2016; Whipple et al., 2000). Lateral erosion is also common during large floods in rapidly incising rivers (Barbour et al., 2009; Beer et al., 2017; Hartshorn et al., 2002; Turowski et al., 2008;), and outburst floods including the Yigong flood and other modern lake-outburst floods are known to have promoted slope failures (e.g., Cook et al., 2018; Larsen & Montgomery, 2012; Turowski et al., 2008). We use simulated flood shear stresses and flow directions to examine the potential for bedrock plucking and channel incision and the relationship between flow conditions and lateral erosion in the Tsangpo Gorge.

Our simulations enable more precise estimates of the spatial distribution of high bed shear stresses and size of transportable blocks for the flood than previously possible. Lang et al. (2013) used estimates of peak discharge and equations for bed shear stress and incipient motion from Lamb, Dietrich, and Venditti (2008) to estimate the size of blocks that could be transported by the Yigong flood and by a megaflood for which discharge had been estimated by Montgomery et al. (2004). However, these calculations relied on gross simplifications of the channel geometry and flow characteristics that poorly approximate flood hydraulics in complex 3-D terrain and provide no information on spatial and temporal variations in transport conditions. For our analysis, we calculated the magnitude, duration, and spatial distribution of bed shear stress as well as Froude number (supporting information equations 4–6) through space and time for the entire flood event; animations of output from the simulation at locations discussed along the flood pathway for flow depth, stress, and Froude number (Movies S1–S8) are available in the supporting information. We also combined simulation results at key locations with recently developed theory for calculating the threshold bed shear stress required to pluck a protruding block of a given size via sliding (Lamb et al., 2015; supporting information equations 9–12).

In the steepest part of the flood pathway in the Po River segment of the Tsangpo Gorge, simulated shear stresses up to 5–20 kPa are capable of plucking meter-scale boulders for multiple hours during the flood. Where the highest bed shear stresses in the model domain are observed (location 1, Figure 6), we explored the potential for the flow to pluck 1-m boulders (corresponding to k_s for our $n = 0.04$ simulations) and 5-m boulders (corresponding to the average median axis length on the largest boulder bar observed on the Po River; Table S4). Calculated bed shear stresses here exceed the peak bed shear stress estimates of Lang et al. (2013) for the flood, and are sufficient to pluck 1-m blocks that protrude by 10%, or 5-m blocks that protrude by 20% (1 m), for over 9 hr during the flood. If 5-m blocks protrude by 10%, the stresses at this location are high enough to enable plucking via sliding for ~5 hr during the flow. These values are four times greater than shear stresses just half a kilometer downstream (location 2, Figure 6), highlighting the spatial heterogeneity of shear stresses within the Gorge. Even in lower-stress regions of the Gorge like location 2, flow conditions are sufficient to pluck 1-m blocks with 10% protrusion for up to 6 hr during the flood.

Lang et al. (2013) used the size of transportable blocks to estimate the length-scale of channel bed lowering during a flood. Following this logic, the 1- to 5-m length-scale of boulders that we estimate could be plucked during the flood would correspond to order 10^2 – 10^3 years of incision given long-term erosion rates of 5–10 km/Myr. However, even though shear stresses are high throughout this steep, narrow river reach, it is unlikely that blocks could be plucked everywhere along the channel bed because bed erosion during large floods is likely to be transport limited (Lamb et al., 2015). Although sediment supply from block entrainment and hillslope failure likely restricts erosion to distinct sections of the channel, our estimates of sustained high shear stress suggest the potential for outburst floods to contribute substantially to rapid channel incision in some areas.

The flood produced sustained high bed shear stresses not only in the steep Tsangpo Gorge, but also immediately downstream of breach, and in isolated locations associated with valley constrictions along the flood pathway. The initial flood wave produces high simulated shear stresses (≥ 5 kPa) over a significant portion of the first ~17 km of the flood on the Yigong River (Movie S2); by about an hour into the flood, the highest shear stresses are restricted to the first 40 km downstream of the breach and to isolated zones where rapid flow is focused at valley constrictions (Movie S2). Two of these high shear stress zones occur at topographic choke points in the Po River segment of the Tsangpo Gorge, 27 and 31 km downstream of the breach (near locations 1–2 discussed previously). Valley constrictions far downstream on the Siang River also produce

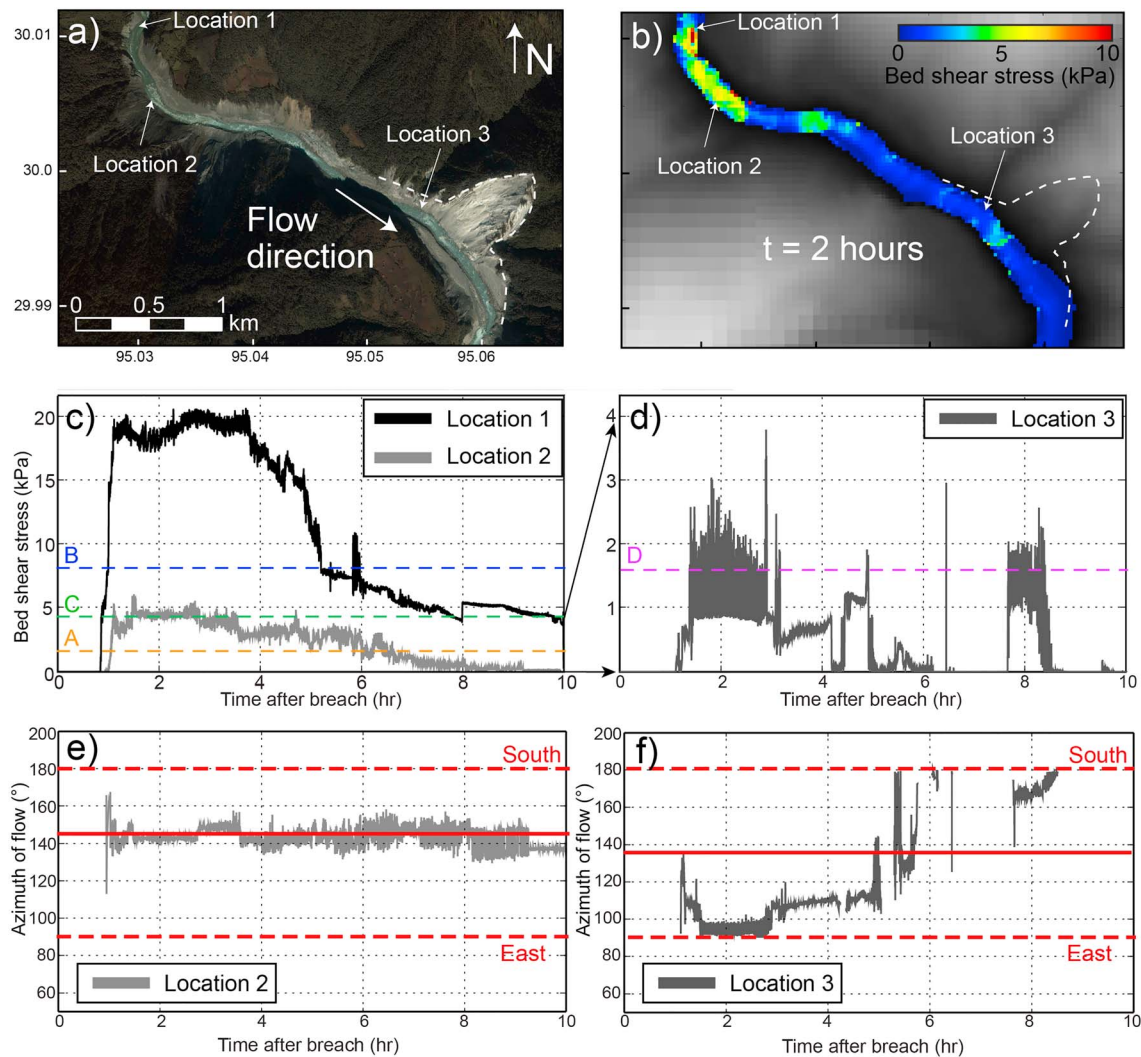


Figure 6. Google Earth image in (a) shows a segment of the Po River with the outline of a large kilometer-scale landslide. Simulated bed shear stress at $t = 2$ hr after the breach is shown in (b). Bed shear stress recorded at locations 1 and 2 is shown in (c) and at location 3 in (d). The orange dotted line A is the threshold bed shear stress for plucking a 1-m block by sliding with 10% protrusion, the blue line B is the threshold stress for plucking a 5-m block by sliding with 10% protrusion, and the green line C is the threshold stress for plucking a 5-m block with 20% protrusion. The purple line in (d) is the threshold stress to pluck a 1-m block with 10% protrusion at location 3 at the toe of the landslide shown in (a). (e) and (f) Azimuth of the flow direction at locations 2 and 3. The solid red line is the orientation of the channel bank at each location, and the dotted red lines show the directions of due east and due south for reference.

zones of high shear stress (Movie S4), including 242 km downstream of the breach near Tuting (Figure 4). The channel gradient at Tuting is an order of magnitude lower than in the Tsangpo Gorge (Figure 1f), yet bed shear stresses at this topographic choke point still exceed 2.5 kPa, which is sufficient to mobilize meter-scale blocks (Figures 7e–7h). These results show the importance of valley morphology in setting up flood hydraulic conditions expected to focus erosion and sediment transport in areas not predicted by patterns of shear stress or stream power for annual flows.

Hydraulic jumps, which are transitions between subcritical and supercritical flow (Froude number > 1) thought to be related to bedrock erosion (Richardson & Carling, 2006; Tinkler & Wohl, 1998; Wilkinson et al., 2018), occur at some choke points (Figure 7h and Movie S8). Such flow features typically develop late in the flow after stage has waned and may persist for many hours, as illustrated by simulation results at a constriction on the Siang River 238 km downstream of the breach that show supercritical flow for 12 hr during the flood (Figure 7h). This hydraulic jump occurs above a ridge that is inundated only at flood stage, and therefore is not a characteristic of monsoon flow. Such simulation results highlight the potential for fast,

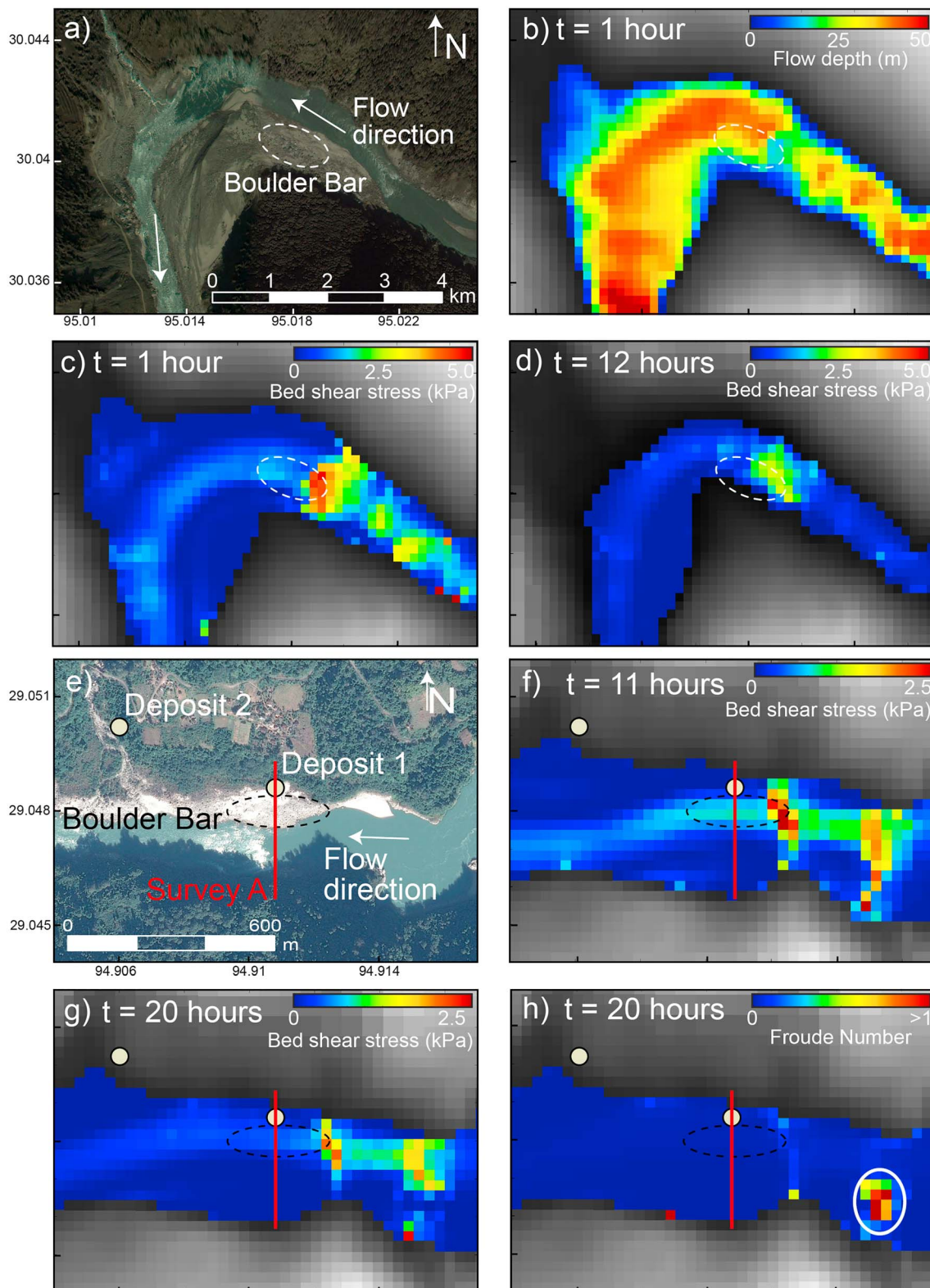


Figure 7. (a) Google Earth image (29 April 2006) showing a large meander on the Po River. Dotted oval shows where boulder size measurements were conducted. (b) Snapshot of simulated water depth at the location in (a) at $t = 1$ hr after the breach. (c and d) Calculated bed shear stress from the simulations at $t = 1$ and 12 hr after the breach. (e) Google Earth image (24 December 2014) showing the Siang River near survey A and boulder bar 238 km downstream from the breach. (f and g) Calculated bed shear stress in the location shown in (e) spaced 1 hr apart that show variations in the distribution of stress in the channel. (h) Froude number map at $t = 20$ hr. Red areas indicate supercritical flow and a hydraulic jump. Scale bar for (b–d) and (f–g) is the same as the Google Earth images.

shallow flow set up by flood-topography interaction to promote bedrock erosion in different zones than would be expected during lower-stage nonflood flows (e.g., Baker, 1973; Malde, 1968).

Finally, we investigated the relationship between simulated flood hydraulics and lateral erosion by examining bed shear stresses adjacent to the 37 large landslides mapped by Larsen and Montgomery (2012) that failed during or shortly after the flood along the Po River segment of the Tsangpo Gorge. The processes of lateral erosion in bedrock rivers are generally not well understood (e.g., Langston & Tucker, 2018). But if plucking was the dominant mechanism for lateral erosion, we might expect slope failures to be focused where high bed shear stresses directed parallel to channel walls act as lever arm to remove blocks. Flow patterns adjacent to over half of the mapped landslides (e.g., location 2, Figure 6e) show high bed shear stresses oriented at a relatively low angle to the channel wall for hours (Table S8), which may facilitate plucking. However, flow at some landslides—including the largest flood-related landslide in the region (location 3, Figure 6f)—is oriented at higher angles to the wall, which may inhibit plucking under high shear stress conditions and potentially facilitate abrasion via impacted particles from upstream.

At the scale of our simulations, 2-D hydraulics vary significantly at the positions of these slope failures, making it difficult to draw conclusions about lateral erosion processes. Higher-resolution topography and computational grids are needed to resolve fine-scale flow features like eddies that are important for abrasion (Carter & Anderson, 2006; Lamb, Dietrich, & Sklar, 2008; Pelletier et al., 2015). Factor-of-safety analysis is needed to assess controls on hillslope stability in addition to oversteepening due to lateral erosion, including changes in pore fluid pressure and cohesion due to flood inundation and vegetation scour. Future work extending this analysis is needed to better resolve topography-flow interactions contributing to lateral erosion and mass wasting during outburst floods.

6.3. Implications of Outburst Flood Hydraulics for Deposition, Bed Armoring, and Channel Roughness

Some studies of ancient outburst floods have related simulated hydraulics to geomorphic features and deposits (e.g., Alho et al., 2010; Bohorquez et al., 2015; Denlinger & O'Connell, 2009; O'Connor, 1993; Komatsu et al., 2009; Larsen & Lamb, 2016; Miyamoto et al., 2006), and recent work on modern outburst floods has begun to examine relationships between hydraulics and geomorphology (e.g., Cook et al., 2018; Kougkoulos et al., 2018). Building on this prior work, we focus on the interaction of the flow with valley topography to address how outburst flood hydraulics relate to slackwater sand and boulder bar deposition, with implications for bed armoring and roughness relevant to long-term river incision.

Simulated flow patterns suggest that the timing of slackwater sand deposition, and the elevation of slackwater deposits relative to peak flood stage, depend on the interaction of flow hydraulics with local valley topography. Some deposits are located on terraces that are only submerged early in the flood near peak inundation. For instance, deposits 3 and 4 on terraces near Tuting (Figures 4 and 5 and Movie S3) are inundated up to 0.1 to 5 m, respectively, from ~2 to 11 hr after the flood wave arrival (Figure S4). Simulated bed shear stresses at deposit 4 are sufficient to suspend the observed 90th percentile grain size (for criteria for suspension see Ferguson & Church, 2004; Bagnold, 1966; supporting information equations 13–15), and fluctuations in flow speed as flood stage wanes are consistent with laminations present in the deposit. The correspondence between simulated hydraulics and characteristics of this and other deposits shows the potential utility of GeoClaw for predicting the location of historical or ancient outburst flood deposits where inundation patterns are unknown (Bohorquez et al., 2015; Denlinger et al., 2002). However, other flood sand deposits are located on surfaces much lower in elevation with respect to the river, where simulated bed shear stresses remain much higher than the threshold for sand suspension until >20 hr after the flood wave arrives (e.g., deposit 1, Figure 5; Movie S4). These observations suggest high concentrations of sand-size sediment were in suspension as the flood waned, and show that the relationship between deposit elevation and maximum stage may vary significantly for a single flood. This finding suggests additional constraints on provenance and/or age may be needed to correlate ancient slackwater deposits recording outburst flood events.

The simulation results also provide evidence of a link between flood hydraulics and the deposition of large boulder bars along the flood pathway. We focus on bars within 320 km of the breach, for which grain sizes of individual boulders can be resolved with Google Earth imagery. The largest boulder bar (>1.5 km length)

occurs near the inside of a meander bend on the Po River. Deposition and point bar formation may be expected at the inside of bends under background discharge conditions. However, the critical stress required for incipient motion of the large boulders on its surface (~ 4.6 kPa for 5-m median intermediate axis; calculations of the shear stress for incipient motion follow Lamb, Dietrich, & Venditti, 2008; supporting information equations 9 and 10) is extremely high, even compared to observations of other outburst floods (e.g., Lamb & Fonstad, 2010). Landsat 7 imagery from before and after the flood, as well as our simulation results, show that the flood inundated this feature, and simulated stresses at the upstream end of the bar exceed the critical stress for incipient motion of 5-m blocks (Figures 7c and 7d and Movie S6). Stress decreases downstream across the bar to values below this threshold for motion, and the stress gradient persists across the boulder bar for >10 hr as stress magnitude wanes. Despite the boulder bar's position near the inside of a channel bend, the large particle sizes and scale of the feature suggest a direct link to outburst floods. We also observed 75 large boulder bars along the pathway that are not located on the inside of meander bends (BoulderBar.kmz). The Siang River boulder bar in Figures 7e–7h is typical of this data set, similar in scale and particle size to the other 66 mapped bars within 320 km of the breach. Simulated flood shear stresses just upstream of this bar exceed the critical stress required for incipient motion (~ 1.6 kPa) of the median intermediate axis size boulder measured here (3 m) (Figures 7f and 7g), and show similar spatial and temporal stress variations as the Po River boulder bar. Bar deposition may be related to complex spatial and temporal variability in hydraulics and transport capacity; nevertheless, our results suggest the magnitude of flood shear stresses is of the right order to be consistent with transport and deposition of the observed size boulders.

Valley topography produces spatial gradients in bed shear stress during outburst floods that we suggest drive deposition of boulder bars that cannot be moved by lower-magnitude background flows, with implications for erosion. Boulder deposition armors the bed, limiting incision in specific locations during nonflood flows (Sklar & Dietrich, 2004; Turowski et al., 2007). Boulder deposition increases channel roughness, extracting momentum from the flow (Chatanantavet & Parker, 2008), further limiting the capacity of the river to transport sediment, expose the bed, and incise in these locations. Increased channel roughness due to boulder bar deposition may also potentially facilitate lateral erosion (Fuller, 2014). The hydraulics of infrequent, high-magnitude floods may therefore exert a strong control on channel incision and development of channel width and the river longitudinal profile. Taken together, our observations highlight the potential for background discharges and outburst floods of different sizes to promote not only different amounts, but also different patterns of bedrock erosion (Reid et al., 2018).

7. Conclusions

We combined field and remote sensing observations with 2-D numerical flood simulations to study the hydraulics and geomorphic impact of a large landslide-dam outburst flood. Simulated hydraulics of the flood, assuming instantaneous dam failure and a range of Manning's n values suitable for natural bedrock channels, are consistent with geomorphic observations of erosion and deposition along >450 km of the flood pathway through the eastern Himalaya. Inundation patterns are consistent with high-water marks >240 km downstream of the breach when we account for monsoon stage at the time of the flood. The accuracy of inundation patterns simulated for this extreme flood over hundreds of kilometers through rugged topography shows that the shallow water equations implemented within GeoClaw can aid in studies of flood hazard, paleoflood reconstruction, and geomorphic processes.

Our proof-of-concept integration of GeoClaw simulations and observations of the Eastern Himalaya provides insights into the control of extreme flood hydraulics on deposition and erosion. Results indicate that the timing and elevation of slackwater sand deposition with respect to peak flood stage vary significantly among the Yigong flood deposits. This finding highlights the potential for slackwater sand deposit elevation to significantly underestimate peak stage, and suggests prehistoric slackwater deposits cannot be correlated based on deposit elevation and simulated inundation patterns in the absence of independent provenance and/or geochronologic constraints. Our flood simulations and observations also provide strong evidence that outburst floods formed numerous large boulder bars along the Tsangpo Gorge and Siang River. We propose that these flood-related deposits armor the bed, increase roughness, and inhibit incision in zones where the interaction of annual flows with topography would not predict boulder deposition.

Immediately downstream of the breach and near valley constrictions in the Tsangpo Gorge and Siang River, simulated shear stresses exceeded the threshold for plucking of meter-scale blocks for multiple hours during the flood. This finding supports the idea that outburst floods may accomplish significant vertical incision into jointed bedrock in detachment-limited reaches of these valleys. However, shear stresses are spatially heterogeneous and vary by a factor of five over distances of less than a kilometer in the Tsangpo Gorge, underscoring the difficulty of equating the length-scale of block plucking with the length-scale of bed incision during an outburst flood. The observation that zones of sustained high shear stress outside the Tsangpo Gorge are associated with valley constrictions points to the potential importance of valley morphology above the channel in controlling outburst flood hydraulics. Future modeling studies are needed to explore the relationship between valley form and hydraulics for different magnitude flows, including Quaternary glacial-lake megafloods through the Tsangpo Gorge. Together with more sophisticated investigation of the interaction of flow hydraulics with slope stability, such work can help quantify how patterns and processes of lateral erosion and incision vary with flood magnitude.

Acknowledgments

We thank Karl Lang, Isaac Larsen, and David Montgomery for field assistance and discussion and acknowledge field support from Oken Tayeng, Tapir Tayeng, and Abor Travels. Joanne Bourgeois, Sarah Schanz, and Susannah Morey provided comments on an earlier draft. We thank Jim O'Connor, Isaac Larsen, an anonymous reviewer, and Mikael Attal for exceptionally helpful reviews. Funding was provided by the Quaternary Research Center at the University of Washington and U.S. National Science Foundation (EAR-1349279, EAR-0955309 to K. W. H.; DMS-1216732 to R. J. L.). Data relevant to methods, tables, and figures are located in the supporting information that accompanies this article. All code can be found in the GitHub repository (<https://github.com/zewski14/YigongGeoClaw>).

References

- Ahlers, R., Budds, J., Joshi, D., Merme, V., & Zwartveene, M. (2014). Framing hydropower as green energy: Assessing drivers, risks and tensions in the Eastern Himalayas. *Earth System Dynamics Discussions*, 5, 1521–1541. <https://doi.org/10.5194/esdd-5-1521-2014>
- Alho, P., & Aaltonen, J. (2008). Comparing a 1D hydraulic model with a 2D hydraulic model for the simulation of extreme glacial outburst floods. *Hydrological Processes: An International Journal*, 22(10), 1537–1547. <https://doi.org/10.1002/hyp.6692>
- Alho, P., Baker, V. R., & Smith, L. N. (2010). Paleohydraulic reconstruction of the largest Glacial Lake Missoula draining (s). *Quaternary Science Reviews*, 29(23–24), 3067–3078. <https://doi.org/10.1016/j.quascirev.2010.07.015>
- Allen, S. K., Linsbauer, A., Huggel, C., Randhawa, S. S., Schaub, Y., & Stoffel, M. (2016). Current and future glacial lake outburst flood hazard: Application of GIS-based modeling in Himachal Pradesh, India. In *Climate change, glacier response, and vegetation dynamics in the Himalaya* (pp. 181–203). Cham: Springer.
- Arcos, M. E. M., & LeVeque, R. J. (2015). Validating velocities in the GeoClaw tsunami model using observations near Hawaii from the 2011 Tohoku tsunami. *Pure and Applied Geophysics*, 172, 849–867. <https://doi.org/10.1007/s00024-014-0980-y>
- Bagnold, R. A. (1966). An approach to the sediment transport problem from general physics. US Geol. Surv. Prof. Pap. 422-I, 1–37.
- Bajracharya, B., Shrestha, A. B., & Rajbhandari, L. (2007). Glacial lake outburst floods in the Sagarmatha region: Hazard assessment using GIS and hydrodynamic modeling. *Mountain Research and Development*, 27(4), 336–344. <https://doi.org/10.1659/mrd.0783>
- Baker, V. (1973). Paleohydrology and sedimentology of the Lake Missoula flooding in eastern Washington. *Geological Society of America Special Papers*, 144, 1–79. <https://doi.org/10.1130/SPE144-p1>
- Baker, V. (2001). Water and the Martian landscape. *Nature*, 412(6843), 228–236. <https://doi.org/10.1038/35084172>
- Baker, V., & Milton, D. (1974). Erosion by catastrophic floods on Mars and Earth. *Icarus*, 23(1), 27–41. [https://doi.org/10.1016/0019-1035\(74\)90101-8](https://doi.org/10.1016/0019-1035(74)90101-8)
- Barbour, J., Stark, C., Lin, C.-W., Chen, H., Horng, M.-J., Ko, C.-P., et al. (2009). Magnitude-frequency distributions of boundary shear stress along a rapidly eroding bedrock river. *Geophysical Research Letters*, 36, L04401. <https://doi.org/10.1029/2008GL035786>
- Bates, P., & De Roo, A. (2000). A simple raster-based model for flood inundation simulation. *Journal of Hydrology*, 236, 54–77. [https://doi.org/10.1016/S0022-1694\(00\)00278-X](https://doi.org/10.1016/S0022-1694(00)00278-X)
- Baynes, E. R. C., Attal, M., Dugmore, A. J., Kirstein, L. A., & Whaler, K. A. (2015). Geomorphology catastrophic impact of extreme flood events on the morphology and evolution of the lower Jökulsá á Fjöllum (northeast Iceland) during the Holocene. *Geomorphology*, 250, 422–436. <https://doi.org/10.1016/j.geomorph.2015.05.009>
- Beer, A., Turowski, J. M., & Kirchner, J. W. (2017). Spatial patterns of erosion in a bedrock gorge. *Journal of Geophysical Research: Earth Surface*, 122, 191–214. <https://doi.org/10.1002/2016JF003850>
- Berger, M. J., George, D. L., LeVeque, R. J., & Mandli, K. T. (2011). The GeoClaw software for depth-averaged flows with adaptive refinement. *Advances in Water Resources*, 34, 1195–1206. <https://doi.org/10.1016/j.advwatres.2011.02.016>
- Bohorquez, P., Carling, P., & Herget, J. (2015). Dynamic simulation of catastrophic late Pleistocene glacial-lake drainage, Altai Mountains, central Asia. *International Geology Review*, 58(14), 1795–1817. <https://doi.org/10.1080/00206814.2015.1046956>
- Booth, A. L., Chamberlain, C. P., Kidd, W. S. F., & Zeitler, P. K. (2009). Constraints on the metamorphic evolution of the eastern Himalayan syntaxis from geochronologic and petrologic studies of Namche Barwa. *Geological Society of America Bulletin*, 121, 385–407. <https://doi.org/10.1130/B26041.1>
- Bracciali, L., Parrish, R. R., Najman, Y., Smye, A., Carter, A., & Wijbrans, J. R. (2016). Plio-Pleistocene exhumation of the eastern Himalayan syntaxis and its domal “pop-up”. *Earth Science Reviews*, 160, 350–385. <https://doi.org/10.1016/j.earscirev.2016.07.010>
- Bretz, J. (1923). The channeled scablands of the Columbia plateau. *The Journal of Geology*, 31(8), 617–649. <https://doi.org/10.1086/623053>
- Burg, J. P., Nievergelt, P., Oberli, F., Seward, D., Davy, P., Maurin, J.-C., et al. (1998). The Namche Barwa syntaxis: Evidence for exhumation related to compressional crustal folding. *Journal of Asian Earth Sciences*, 16, 239–252. [https://doi.org/10.1016/S0743-9547\(98\)00002-6](https://doi.org/10.1016/S0743-9547(98)00002-6)
- Canuti, P., Frassoni, A., & Natale, L. (1994). Failure of the Rio Paute landslide dam. *Landslide News*, 8, 6–7.
- Carling, P., Villanueva, I., Herget, J., Wright, N., Borodavko, P., & Morvan, H. (2010). Unsteady 1D and 2D hydraulic models with ice-dam break for quaternary megaflood, Altai Mountains, southern Siberia. *Global and Planetary Change*, 70(1), 24–34. <https://doi.org/10.1016/j.gloplacha.2009.11.005>
- Carling, P. A. (1996a). Morphology, sedimentology and palaeohydraulic significance of large gravel dunes, Altai Mountains, Siberia. *Sedimentology*, 43(4), 647–664. <https://doi.org/10.1111/j.1365-3091.1996.tb02184.x>
- Carling, P. A. (1996b). A preliminary palaeohydraulic model applied to late-quaternary gravel dunes: Altai mountains, Siberia. In J. Branson, K. J. Gregory, & A. D. Brown (Eds.), *Global continental changes: The context of palaeohydrology*, *Journal of Geology, Geological Society of London Special Publication* (Vol. 115, pp. 165–179).
- Carrivick, J. L. (2006). Application of 2D hydrodynamic modelling to high-magnitude outburst floods: An example from Kverkfjöll, Iceland. *Journal of Hydrology*, 321(1–4), 187–199. <https://doi.org/10.1016/j.jhydrol.2005.07.042>

- Carter, C. L., & Anderson, R. S. (2006). Fluvial erosion of physically modeled abrasion dominated slot canyons. *Geomorphology*, *81*(1–2), 89–113. <https://doi.org/10.1016/j.geomorph.2006.04.006>
- Chapman, M. G., Gudmundsson, M. T., Russell, A. J., & Hare, T. M. (2003). Possible Juventae Chasma sub ice volcanic eruptions and Maja Valles ice outburst floods on Mars: Implications of Mars Global Surveyor crater densities, geomorphology, and topography. *Journal of Geophysical Research*, *108*, 5113. <https://doi.org/10.1029/2002JE002009>
- Chatanantavet, P., & Parker, G. (2008). Experimental study of bedrock channel alluviation under varied sediment supply and hydraulic conditions. *Water Resources Research*, *44*, W12446. <https://doi.org/10.1029/2007WR006581>
- Chen, Y., Aitchison, J. C., Zong, Y., & Li, S. H. (2016). OSL dating of past lake levels for a large dammed lake in southern Tibet and determination of possible controls on lake evolution. *Earth Surface Processes and Landforms*, *41*(11), 1467–1476. <https://doi.org/10.1002/esp.3907>
- Chen, Y., Huang, S., Lin, Y., Liu, J., Chung, L., Lai, K., et al. (2008). Holocene megafloods? Stories of the lacustrine strata along the Nyang River, Tibet: American Geophysical Union Fall Meeting 2008, abs. PP21A-1404.
- Clarke, G. K., Leverington, D. W., Teller, J. T., & Dyke, A. S. (2004). Paleohydraulics of the last outburst flood from glacial Lake Agassiz and the 8200 BP cold event. *Quaternary Science Reviews*, *23*(3–4), 389–407. <https://doi.org/10.1016/j.quascirev.2003.06.004>
- Clawpack Development Team. (2017). Clawpack Version 5.3.0, <http://www.clawpack.org>. doi:<https://doi.org/10.5281/zenodo.262111>.
- Cook, A., & Merwade, V. (2009). Effect of topographic data, geometric configuration and modeling approach on flood inundation mapping. *Journal of Hydrology*, *377*(1–2), 131–142.
- Cook, K. L., Andermann, C., Gimbert, F., Adhikari, B. R., & Hovius, N. (2018). Glacial lake outburst floods as drivers of fluvial erosion in the Himalaya. *Science*, *362*(6410), 53–57. <https://doi.org/10.1126/science.aat4981>
- Costa, J. E. (1988). Floods from dam failures. In V. R. Baker, R. C. Kochel, & P. C. Patton (Eds.), *Flood Geomorphology* (pp. 439–463).
- Costa, J. E., & Schuster, R. L. (1988). The formation and failure of natural dams. *Geological Society of America Bulletin*, *100*, 1054–1068. [https://doi.org/10.1130/0016-7606\(1988\)100<1054:TFAFON>2.3.CO;2](https://doi.org/10.1130/0016-7606(1988)100<1054:TFAFON>2.3.CO;2)
- Costa, J. E., & Schuster, R. L. (1991). Documented historical landslide dams from around the world. U.S. Geological Survey Open-File Report 91–239.
- Datta, B., & Singh, V. P. (2004). In V. P. Singh, et al. (Eds.), *Hydrology in the Brahmaputra basin water resources* (pp. 139–195). Dordrecht, Boston: Kluwer Academic Publishers.
- de Ferranti, J. (2014). 3-arc second digital elevation data. <http://viewfinderpanoramas.org/dem3.html>
- Delaney, K. B., & Evans, S. G. (2015). The 2000 Yigong landslide (Tibetan plateau), rockslide-dammed lake and outburst flood: Review, remote sensing analysis, and process modelling. *Geomorphology*, *246*, 377–393. <https://doi.org/10.1016/j.geomorph.2015.06.020>
- Denlinger, R. P., & O'Connell, D. R. H. (2009). Simulations of cataclysmic outburst floods from Pleistocene Glacial Lake Missoula. *Geological Society of America Bulletin*, *122*(5–6), 678–689. <https://doi.org/10.1130/B26454.1>
- Denlinger, R. P., O'Connell, D. R. H., & House, P. K. (2002). Robust determination of stage and discharge: An example from an extreme flood on the Verde River, Arizona. In R. H. Webb, et al. (Eds.), *Ancient floods and modern hazards: principles and application of paleoflood hydrology* (Vol. 5, pp. 127–146). Washington DC: American Geophysical Union. <https://doi.org/10.1029/WS005p0127>
- Ding, L., Zhong, D., Yin, A., Kapp, P., & Harrison, T. M. (2001). Cenozoic structural and metamorphic evolution of the eastern Himalayan syntaxis (Namche Barwa). *Earth and Planetary Science Letters*, *192*, 423–438. [https://doi.org/10.1016/S0012-821X\(01\)00463-0](https://doi.org/10.1016/S0012-821X(01)00463-0)
- Evans, S. G. (1986). The maximum discharge of outburst floods caused by the breaching of man-made and natural dams. *Canadian Geotechnical Journal*, *23*, 385–387. <https://doi.org/10.1139/t86-053>
- Evans, S. G., & Delaney, K. B. (2011). Characterization of the 2000 Yigong Zangbo River (Tibet) landslide dam and impoundment by remote sensing. In S. Evans, et al. (Eds.), *Natural and artificial rockslide dams* (Vol. 133, pp. 543–559). Berlin, Heidelberg: Springer. https://doi.org/10.1007/978-3-642-04764-0_22
- Ferguson, R. I., & Church, M. (2004). A simple universal equation for grain settling velocity. *Journal of Sedimentary Research*, *74*(6), 933–937. <https://doi.org/10.1306/051204740933>
- Finnegan, N. J., Hallet, B., Montgomery, D. R., Zeitler, P. K., Stone, J. O., Anders, A. M., & Yuping, L. (2008). Coupling of rock uplift and river incision in the Namche Barwa-Gyala Peri massif, Tibet. *Geological Society of America Bulletin*, *120*(1–2), 142–155. <https://doi.org/10.1130/B26224.1>
- Frey, H., Huggel, C., Baer, P., Chisolm, R. E., McArdell, B., Cochachin, A., & Portocarrero, C. (2018). Multi-source glacial lake outburst flood hazard assessment and mapping for Huaraz, Cordillera Blanca, Peru. *Frontiers in Earth Science*, *6*, 210. <https://doi.org/10.3389/feart.2018.00210>
- Froehlich, D. C. (2016). Predicting peak discharge from gradually breached embankment dam. *Journal of Hydrologic Engineering*, *21*(11), 04016041. [https://doi.org/10.1061/\(ASCE\)HE.1943-5584.0001424](https://doi.org/10.1061/(ASCE)HE.1943-5584.0001424)
- Fuller, T.K. (2014). Field, experimental and numerical investigations into the mechanisms and drivers of lateral erosion in bedrock channels. (PhD). University of Minnesota, Minneapolis, MN.
- Galland, J. C., Goutal, N., & Hervouet, J.-M. (1991). TELEMAT—A new numerical-model for solving shallow-water equations. *Advances in Water Resources*, *14*(3), 138–148. [https://doi.org/10.1016/0309-1708\(91\)90006-A](https://doi.org/10.1016/0309-1708(91)90006-A)
- García-Castellanos, D., & O'Connor, J. E. (2018). Outburst floods provide erodability estimates consistent with long-term landscape evolution. *Scientific Reports*, *8*(1), 10573. <https://doi.org/10.1038/s41598-018-28981-y>
- George, D. L. (2011). Adaptive finite volume methods with well-balanced Riemann solvers for modeling floods in rugged terrain: Application to the Malpasset dam-break flood (France, 1959). *International Journal for Numerical Methods in Fluids*, *66*(8), 1000–1018. <https://doi.org/10.1002/flid.2298>
- Goudge, T. A., & Fassett, C. I. (2018). Incision of Licus Vallis, Mars, from multiple lake overflow floods. *Journal of Geophysical Research: Planets*, *123*, 405–420. <https://doi.org/10.1002/2017JE005438>
- Guangxiang, Y., & Qingli, Z. (2012). Glacier-dammed Lake in southeastern Tibetan plateau during the last glacial maximum. *Journal of Geological Society of India*, *79*, 295–301. <https://doi.org/10.1007/s12594-012-0041-z>
- Guangxiang, Z., & Xitao, S. (2007). Songzong Lake: An ice-dammed lake of last glacial maximum in Purlung Tsangpo River, Southeast Tibet. *Quaternary Sciences*, *1*, 009.
- Han, Z. S. (2003). Large-scale landslide-debris avalanche in Tibet, China (1) April–June 2000 Yigong landslide, Tibet China. *Landslide News*, *14–15*, 22–23.
- Hartshorn, K., Hovius, N., Dade, W. B., & Slingerland, R. L. (2002). Climate-driven bedrock incision in an active mountain belt. *Science*, *297*, 2036–2038. <https://doi.org/10.1126/science.1075078>
- Henderson, F. M. (1966). *Flow resistance in open channel flow* (pp. 96–101). New York: MacMillan Publishing CO.
- Hewitt, K. (1968). Record of natural damming and related floods in the Upper Indus Basin. *Indus*, *10*(3), 11–19.

- Horritt, M. S., & Bates, P. D. (2002). Evaluation of 1D and 2D numerical models for predicting river flood inundation. *Journal of Hydrology*, 268(1-4), 87–99. [https://doi.org/10.1016/S0022-1694\(02\)00121-X](https://doi.org/10.1016/S0022-1694(02)00121-X)
- Hu, H. P., Feng, J. L., & Chen, F. (2018). Sedimentary records of a palaeo-lake in the middle Yarlung Tsangpo: Implications for terrace genesis and outburst flooding. *Quaternary Science Reviews*, 192, 135–148. <https://doi.org/10.1016/j.quascirev.2018.05.037>
- Huang, S.-Y., Chen, Y.-G., Burr, G. S., Jaiswal, M. K., Lin, Y. N., Yin, G., et al. (2014). Late Pleistocene sedimentary history of multiple glacially dammed lake episodes along the Yarlung-Tsangpo river, southeast Tibet. *Quaternary Research*, 82, 430–440. <https://doi.org/10.1016/j.yqres.2014.06.001>
- Kaiser, K., Lai, Z., Schneider, B., & Junge, F. W. (2010). Late Pleistocene genesis of the middle Yarlung Zangbo Valley, southern Tibet (China), as deduced by sedimentological and luminescence data. *Quaternary Geochronology*, 5(2–3), 200–204. <https://doi.org/10.1016/j.quageo.2009.01.005>
- King, J., Loveday, I., & Schuster, R. L. (1989). The 1985 Bairaman landslide dam and resulting debris flow, Papua New Guinea. *Quarterly Journal of Engineering Geology, London*, 22, 257–270. <https://doi.org/10.1144/GSL.QJEG.1989.022.04.02>
- Komatsu, G., Arzhannikov, S. G., Gillespie, A. R., Burke, R. M., Miyamoto, H., & Baker, V. R. (2009). Quaternary paleolake formation and cataclysmic flooding along the upper Yenisei River. *Geomorphology*, 104, 143–164. <https://doi.org/10.1016/j.geomorph.2008.08.009>
- Korup, O. (2002). Recent research on landslide dams: a literature review with special attention to New Zealand. *Progress in Physical Geography*, 26, 206–235. <https://doi.org/10.1191/0309133302pp333ra>
- Korup, O. (2005). Geomorphic hazard assessment of landslide dams in South Westland, New Zealand: Fundamental problems and approaches. *Geomorphology*, 66, 167–188. <https://doi.org/10.1016/j.geomorph.2004.09.013>
- Korup, O., & Montgomery, D. R. (2008). Tibetan plateau river incision inhibited by glacial stabilization of the Tsangpo gorge. *Nature*, 455(7214), 786–789. <https://doi.org/10.1038/nature07322>
- Korup, O., Montgomery, D. R., & Hewitt, K. (2010). Glacier and landslide feedbacks to topographic relief in the Himalayan syntaxes. *Proceedings of the National Academy of Sciences of the United States of America*, 107(12), 5317–5322. <https://doi.org/10.1073/pnas.0907531107>
- Koukoulou, I., Cook, S. J., Edwards, L. A., Clarke, L. J., Symeonakis, E., Dortch, J. M., & Nesbitt, K. (2018). Modelling glacial lake outburst flood impacts in the Bolivian Andes. *Natural Hazards*, 1–24.
- Lamb, M., Dietrich, W., Aciego, S., Depaolo, D., & Manga, M. (2008). Formation of Box Canyon, Idaho, by megaflood: Implications for seepage erosion on Earth and Mars. *Science*, 320(5879), 1067–1070. <https://doi.org/10.1126/science.1156630>
- Lamb, M., & Fonstad, M. (2010). Rapid formation of a modern bedrock canyon by a single flood event. *Nature Geoscience*, 3(7), 477–481. <https://doi.org/10.1038/NGE0894>
- Lamb, M. P., Dietrich, W. E., & Sklar, L. S. (2008). A model for fluvial bedrock incision by impacting suspended and bed load sediment. *Journal of Geophysical Research*, 113, F03025. <https://doi.org/10.1029/2007JF000915>
- Lamb, M. P., Dietrich, W. E., & Venditti, J. G. (2008). Is the critical shields stress for incipient sediment motion dependent on channel-bed slope? *Journal of Geophysical Research*, 113, F02008. <https://doi.org/10.1029/2007JF000831>
- Lamb, M. P., Finnegan, N. J., Scheingross, J. S., & Sklar, L. S. (2015). New insights into the mechanics of fluvial bedrock erosion through flume experiments and theory. *Geomorphology*, 244, 33–55. <https://doi.org/10.1016/j.geomorph.2015.03.003>
- Lang, K. A., Huntington, K. W., Burmester, R., & Housen, B. (2016). Rapid exhumation of the eastern Himalayan syntaxis since the Late Miocene. *Geological Society of America Bulletin*, 128, 1403–1422. <https://doi.org/10.1130/B31419.1>
- Lang, K. A., Huntington, K. W., & Montgomery, D. R. (2013). Erosion of the Tsangpo Gorge by megafloods, Eastern Himalaya. *Geology*, 41(9), 1003–1006. <https://doi.org/10.1130/G34693.1>
- Langston, A. L., & Tucker, G. E. (2018). Developing and exploring a theory for the lateral erosion of bedrock channels for use in landscape evolution models. *Earth Surface Dynamics*, 6(1), 1–27. <https://doi.org/10.5194/esurf-6-1-2018>
- Larsen, I. J., & Lamb, M. (2016). Progressive incision of the channeled scablands by outburst floods. *Nature*, 538(7624), 229–232. <https://doi.org/10.1038/nature19817>
- Larsen, I. J., & Montgomery, D. R. (2012). Landslide erosion coupled to tectonics and river incision. *Nature Geoscience*, 5(7), 468–473. <https://doi.org/10.1038/NGE01479>
- LeVeque, R. J., George, D. L., & Berger, M. J. (2011). Tsunami modeling with adaptively refined finite volume methods. *Acta Numerica*, 211–289. <https://doi.org/10.1017/S0962492911000043>
- Liu, W., Lai, Z., Hu, K., Ge, Y., Cui, P., Zhang, X., & Liu, F. (2015). Age and extent of a giant glacial-dammed lake at Yarlung Tsangpo gorge in the Tibetan Plateau. *Geomorphology*, 246, 370–376. <https://doi.org/10.1016/j.geomorph.2015.06.034>
- Liu, W., Zhou, G. G., Ge, Y., & Huang, R. (2018). Gradual late stage deepening of Gega ice-dammed lake, Tsangpo gorge, southeastern Tibet, indicated by preliminary sedimentary rock magnetic properties. *Acta Geophysica*, 1–8.
- Liu, Y., Montgomery, D. R., Hallet, B., Tang, W., Zhang, J. L., & Zhang, X. Y. (2006). Quaternary glacier blocking events at the entrance of Yarlung Zangbo Great Canyon, Southeast Tibet. *Quaternary Sciences*, 26(1), 52–62.
- Macinnes, B. T., Gusman, A. R., Leveque, R. J., & Tanioka, Y. (2013). Comparison of earthquake source models for the 2011 Tohoku event using tsunami simulations and near-field observations. *Bulletin of the Seismological Society of America*, 103(2), 1256–1274. <http://doi.org/10.1785/0120120121>
- Malde, H. (1968). The catastrophic late Pleistocene Bonneville flood in the Snake River Plain, Idaho. USGS Professional Paper, 596, pp. 1–52.
- Malloy, M. (2004). Rapid erosion at the Tsangpo knickpoint and exhumation of southeastern Tibet [M.S. thesis]: Lehigh University, 82 p.
- Mandli, K. T., Ahmadi, A. J., Berger, M., Calhoun, D., George, L., Hadjimichael, Y., et al. (2016). Clawpack: Building on an open source ecosystem for solving hyperbolic PDEs. *PeerJ Computer Science*, 1–27. <https://doi.org/10.7717/peerj-cs.68>
- Manning, R. (1891). On the flow of water in open channels and pipes. *Transactions, Institution of Civil Engineers of Ireland*, 20, 161–207.
- Miyamoto, H., Itoh, K., Komatsu, G., Baker, V., Dohm, J., Tosaka, H., & Sasaki, S. (2006). Numerical simulations of large-scale cataclysmic floodwater: A simple depth-averaged model and an illustrative application. *Geomorphology*, 76(1-2), 179–192. <https://doi.org/10.1016/j.geomorph.2005.11.002>
- Montgomery, D. R., Hallet, B., Yuping, L., Finnegan, N., Anders, A., Gillespie, A., & Greenberg, H. M. (2004). Evidence for Holocene megafloods down the Tsangpo River gorge, southeastern Tibet. *Quaternary Research*, 62(02), 201–207. <https://doi.org/10.1016/j.yqres.2004.06.008>
- O'Connor, J. (1993). Hydrology, hydraulics, and geomorphology of the Bonneville flood. *Geological Society of America Special Papers*, 274, 1–83. <https://doi.org/10.1130/SPE274-p1>

- O'Connor, J. E., & Baker, V. R. (1992). Magnitudes and implications of peak discharges from glacial Lake Missoula. *Geological Society of America Bulletin*, 104(3), 267–279. [https://doi.org/10.1130/0016-7606\(1992\)104<0267:MAIOPD>2.3.CO;2](https://doi.org/10.1130/0016-7606(1992)104<0267:MAIOPD>2.3.CO;2)
- O'Connor, J. E., & Beebee, R. A. (2009). Floods from natural rock-material dams. In P. A. Carling, & V. R. Baker (Eds.), *Burr, DM* (pp. 128–171). Megaflooding on Earth and Mars, Cambridge: Cambridge University Press.
- O'Connor, J. E., Clague, J. J., Walder, J. S., Manville, V., & Beebee, R. A. (2013). In J. F. Shroder (Ed.), *Outburst floods in treatise on geomorphology* (Vol. 9, pp. 475–510). San Diego California: Academic Press.
- Pelletier, J. D., Sweeney, K. E., Roering, J. J., & Finnegan, N. J. (2015). Controls on the geometry of potholes in bedrock channels. *Geophysical Research Letters*, 42, 797–803. <https://doi.org/10.1002/2014GL062900>
- Plaza-Nieto, G., Yepes, H., & Schuster, R. L. (1990). Landslide dam on the Pisque River, northern Ecuador. *Landslide News*, 4, 2–4.
- Reid, H. E., Williams, R. D., Brierley, G. J., Coleman, S. E., Lamb, R., & Rennie, C. D. (2018). Geomorphological effectiveness of floods to rework gravel bars: Insight from hyperscale topography and hydraulic modelling. *Earth Surface Processes and Landforms*, 44(2), 595–613. <https://doi.org/10.1002/esp.4521>
- Richardson, K., & Carling, P. A. (2006). The hydraulics of a straight bedrock channel: Insights from solute dispersion studies. *Geomorphology*, 82(1-2), 98–125. <https://doi.org/10.1016/j.geomorph.2005.09.022>
- Richardson, S. D., & Reynolds, J. M. (2000). An overview of glacial hazards in the Himalayas. *Quaternary International*, 65(66), 31–47. [https://doi.org/10.1016/S1040-6182\(99\)00035-X](https://doi.org/10.1016/S1040-6182(99)00035-X)
- Risley, J. C., Walder, J. S., & Denlinger, R. P. (2006). Usui dam wave overtopping and flood routing in the Bartang and Panj Rivers, Tajikistan. *Natural Hazards*, 38(3), 375–390. <https://doi.org/10.1007/s11069-005-1923-9>
- Roberts, S., Nielsen, O., Gray, D., Sexton, J., & Davies, G. (2015). ANUGA user manual. Release 2.0. https://github.com/GeoscienceAustralia/anuga_core/raw/master/doc/anuga_user_manual.pdf
- Ruiz-Villanueva, V., Allen, S., Arora, M., Goel, N. K., & Stoffel, M. (2017). Recent catastrophic landslide lake outburst floods in the Himalayan mountain range. *Progress in Physical Geography*, 41(1), 3–28. <https://doi.org/10.1177/0309133316658614>
- Salvatore, G., Andrea, P., Ettore, A., & Nardi, F. (2013). Flood mapping in ungagged basins using fully continuous hydrologic-hydraulic modeling. *Journal of Hydrology*, 487, 39–47.
- Sattar, A., Goswami, A., & Kulkarni, A. V. (2018). Hydrodynamic modeling of glacial lake outburst flood (GLOF) and its impact on a hydropower station—A case study at the upper Alaknanda Basin, Central Himalaya. In EGU General Assembly Conference Abstracts (Vol. 20, p. 1575).
- Schneider, D., Huggel, C., Cochachin, A., Guillén, S., & García, J. (2014). Mapping hazards from glacier lake outburst floods based on modelling of process cascades at lake 513, Carhuaz, Peru. *Advances in Geosciences*, 35, 145–155. <https://doi.org/10.5194/adgeo-35-145-2014>
- Schwanghart, W., Ryan, M., & Korup, O. (2018). Topographic and seismic constraints on the vulnerability of Himalayan hydropower. *Geophysical Research Letters*, 45, 8985–8992. <https://doi.org/10.1029/2018GL079173>
- Schwanghart, W., Worni, R., Huggel, C., Stoffel, M., & Korup, O. (2016). Uncertainty in the Himalayan energy–water nexus: Estimating regional exposure to glacial lake outburst floods. *Environmental Research Letters*, 11(7), 074005. <https://doi.org/10.1088/1748-9326/11/7/074005>
- Seward, D., & Burg, J. (2008). Growth of the Namche Barwa Syntaxis and associated evolution of the Tsangpo Gorge: Constraints from structural and thermochronological data. *Tectonophysics*, 451, 282–289. <https://doi.org/10.1016/j.tecto.2007.11.057>
- Shang, Y., Yang, Z., Li, L., Liu, D., Liao, Q., & Wang, Y. (2003). A super-large landslide in Tibet in 2000: Background, occurrence, disaster, and origin. *Geomorphology*, 54(3–4), 225–243. [https://doi.org/10.1016/S0169-555X\(02\)00358-6](https://doi.org/10.1016/S0169-555X(02)00358-6)
- Shean, D. (2017). High mountain Asia 8-meter DEM mosaics derived from optical imagery, Version 1. Boulder, Colorado USA. NASA National Snow and Ice Data Center Distributed Active Archive Center.
- Shrestha, A. B., Eriksson, M., Mool, P., Ghimire, P., Mishra, B., & Khanal, N. R. (2010). Glacial lake outburst flood risk assessment of Sun Koshi basin, Nepal. *Geomatics, Natural Hazards and Risk*, 1(2), 157–169. <https://doi.org/10.1080/19475701003668968>
- Sklar, L. S., & Dietrich, W. E. (2004). A mechanistic model for river incision into bedrock by saltating bed load. *Water Resources Research*, 40, W06301. <https://doi.org/10.1029/2003WR002496>
- Tewari, P. (2004). A study of soil erosion in Pasighat town (Arunachal Pradesh) India. *Natural Hazards*, 32, 257–275. <https://doi.org/10.1023/B:NHAZ.0000031317.69865.b7>
- Tinkler, K. J., & Wohl, E. (1998). A primer on bedrock channels. In K. J. Tinkler, & E. E. Wohl (Eds.), *Rivers over Rock: Fluvial processes in bedrock channels*, *Geophysical Monograph Series* (Vol. 107, pp. 1–18). Washington DC: American Geophysical Union. <https://doi.org/10.1029/GM107p0001>
- Turowski, J. M., Hovius, N., Meng-Long, H., Lague, D., & Men-Chiang, C. (2008). Distribution of erosion across bedrock channels. *Earth Surface Processes and Landforms*, 33, 353–363. <https://doi.org/10.1002/esp.1559>
- Turowski, J. M., Lague, D., & Hovius, N. (2007). Cover effect in bedrock abrasion: A new derivation and its implications for the modeling of bedrock channel morphology. *Journal of Geophysical Research*, 112, F04006. <https://doi.org/10.1029/2006JF000697>
- Walder, J. S., & O'Connor, J. E. (1997). Methods for predicting peak discharge of floods caused by failure of natural and constructed earthen dams. *Water Resources Research*, 33(10), 2337–2348. <https://doi.org/10.1029/97WR01616>
- Wang, W., Gao, Y., Anaconda, P. I., Lei, Y., Xiang, Y., Zhang, G., et al. (2018). Integrated hazard assessment of Cirenmaco glacial lake in Zhangzangbo valley, Central Himalayas. *Geomorphology*, 306, 292–305. <https://doi.org/10.1016/j.geomorph.2015.08.013>
- Weidinger, J. T. (2006). Landslide dams in the high mountains of India, Nepal and China: Stability and life span of their dammed lakes. *Italian Journal of Engineering Geology and Environment*, 1, 67–80. <https://doi.org/10.4408/IJEGE.2006-01.S-08>
- Westoby, M. J., Brasington, J., Glasser, N. F., Hambrey, M. J., Reynolds, J. M., Hassan, M. A. A. M., & Lowe, A. (2015). Numerical modelling of glacial lake outburst floods using physically based dam-breach models. *Earth Surface Dynamics*, 3(1), 171–199. <https://doi.org/10.5194/esurf-3-171-2015>
- Westoby, M. J., Glasser, N. F., Brasington, J., Hambrey, M. J., Quincey, D. J., & Reynolds, J. M. (2014). Modelling outburst floods from moraine-dammed glacial lakes. *Earth-Science Reviews*, 134, 137–159. <https://doi.org/10.1016/j.earscirev.2014.03.009>
- Whipple, K. X., Hancock, G. S., & Anderson, R. S. (2000). River incision into bedrock: Mechanics and relative efficacy of plucking, abrasion, and cavitation. *Geological Society of America Bulletin*, 112(3), 490–503. [https://doi.org/10.1130/0016-7606\(2000\)112<490:RIIBMA>2.0.CO;2](https://doi.org/10.1130/0016-7606(2000)112<490:RIIBMA>2.0.CO;2)
- Wilkinson, C., Harbor, D. J., Helgans, E., & Kuehner, J. P. (2018). Plucking phenomena in nonuniform flow. *Geosphere*, 14(5), 2157–2170. <https://doi.org/10.1130/GES01623.1>
- Worni, R., Huggel, C., & Stoffel, M. (2013). Glacial lakes in the Indian Himalayas: From an area-wide glacial lake inventory to on-site and modeling based risk assessment of critical glacial lakes. *Science of the Total Environment*, 468, S71–S84. <https://doi.org/10.1016/j.scitotenv.2012.11.043>

- Xu, Q., Fan, X. M., Huang, R. Q., & Van Westen, C. (2009). Landslide dams triggered by the Wenchuan earthquake, Sichuan Province, south west China. *Bulletin of Engineering Geology and the Environment*, 68(3), 373–386. <https://doi.org/10.1007/s10064-009-0214-1>
- Yang, X., Yang, Z., Cao, S., Gao, X., & Li, S. (2010). Key techniques for the emergency disposal of Quake Lakes. *Natural Hazards*, 52, 43–56. <https://doi.org/10.1007/s11069-009-9350-y>
- Zeitler, P., Meltzer, A., Brown, L., Kidd, W., Lim, C., & Enkelmann, E. (2014). Tectonics and topographic evolution of Namche Barwa and the easternmost Lhasa Block, Tibet. In J. Nie, B. K. Hortonm, & G. D. Hoke (Eds.), *Toward an Improved Understanding of Uplift Mechanisms and the Elevation History of the Tibetan Plateau, Special Paper - Geological Society of America* (Vol. 507, pp. 23–58). [https://doi.org/10.1130/2014.2507\(02\)](https://doi.org/10.1130/2014.2507(02))
- Zhu, P. Y., & Li, T. (2000/2001). Flash flooding caused by landslide dam failure. *Newsletter of ICIMOD*, 38, 4–5.
- Zhu, P. Y., Wang, C. H., & Wang, Y. C. (2003). Large-scale landslide-debris avalanche in Tibet, China; 2, Formation of an exceptionally serious outburst flood from a landslide dam in Tibet. *Landslide News*, 14–15, 23–25.
- Zhu, S., Wu, Z., Zhao, X., Li, J., & Xiao, K. (2014). Ages and genesis of terrace flights in the middle reaches of the Yarlung Zangbo River, Tibetan Plateau, China. *Boreas*, 43(2), 485–504. <https://doi.org/10.1111/bor.12050>
- Zhu, S., Wu, Z. H., Zhao, X. T., Wang, C. M., & Xiao, K. Y. (2013). The age of glacial dammed lakes in the Yarlung Zangbo River Grand Bend during late Quaternary by OSL. *Diqiu Xuebao (Acta Geoscientica Sinica)*, 34(2), 246–250.
- Zin, W. W., Kawasaki, A., Takeuchi, W., San, Z. M. L. T., Htun, K. Z., Aye, T. H., & Win, S. (2018). Flood hazard assessment of Bago River Basin, Myanmar. *Journal of Disaster Research*, 13(1), 15.